SDR Implemented Ground-based Interferometric Radar for Displacement Measurement

Weike Feng *Member, IEEE,* Jean-Michel Friedt

***Abstract*—We demonstrate in this paper the use of general Software Defined Radio (SDR) hardware for ground-based interferometric radar (GBIR) system development for static target imaging and displacement estimation purposes. Firstly, a system synchronization approach is proposed within the free and open-source framework GNU Radio, followed by a frequency-domain bandwidth synthesis method to improve the range resolution using different waveforms. Secondly, data preprocessing and target imaging methods are proposed to reduce the negative influences of practical non-ideal factors and to get high-quality target images. Last, various experiments are conducted to show the performance of the developed SDR-GBIR system and the proposed methods. It is shown that high-resolution target image and high-accuracy displacement measurement can be obtained by our two SDR-GBIR systems: ground-based synthetic aperture radar (SDR-GB-SAR) and ground-based multiple-input-multiple-output (SDR-GB-MIMO) radar.**

***Index Terms*—Software defined radio, Ground-based interferometric radar, Radar imaging, Displacement measurement.**

I. Introduction

Over the last two decades, ground-based interferometric radar (GBIR) has been extensively applied for contact-less, real-time, continuous, high-resolution, and high-accuracy displacement measurements of geophysical (landslide or volcano) and man-made (bridge or dam) structures [1]–[4]. Compared with conventional displacement measurement methods, such as geodetic and laser scanning methods [5], from a single position (maybe outside from the Area of Interest – AoI), GBIR can observe a longer distance, has a larger space coverage, and is able to work days-and-nights in all weather conditions. Compared with space-borne interferometric radar [6], [7], its higher data sampling rate and higher spatial resolution make GBIR preferable for real-time displacement monitoring of a local area. Besides, without of orbit limitation, GBIR can be installed at almost any selected position to have an optimal observation angle to extract useful displacement information of the illuminating scene.

For GBIR, imaging resolutions in range, azimuth, and elevation directions are important to distinguish different targets in the AoI with potential displacements. In order to obtain high range resolution, the simple approach is to increase the bandwidth of the transmitted signal, and, to achieve high cross-range resolutions, synthetic aperture radar (SAR) technique [8] or multiple-input-multiple-output (MIMO) radar technique [9] is normally used, resulting in various GB-SAR and GB-MIMO radar systems. Representatives of GB-SAR systems are [10]–[14]: LISA system from Joint Research Centre (JRC) of the European Commission, IBIS system from IDS GeoRadar company, Fast-GBSAR system from MetaSensing company, GB-NWSAR system from Institute for radiophysics and electronics, and Arc-SAR system from Chinese Academy of Sciences. On the other hand, representatives of GB-MIMO radar systems are [15]–[19]: Melissa system from JRC of the European Commission, MIMO-SAR system from Beijing Institute of Technology, SPARX system from IDS GeoRadar company, compressive sensing (CS) based MIMO radar system from University of Florence, and cross-MIMO radar system from Tohoku University.

Although the theoretical research and practical applications of GB-SAR and GB-MIMO radar are fruitful, some limitations exist. On the one hand, exiting GB-SAR and GB-MIMO radar systems are highly specialized and integrated, developed for specific tasks. The lack of universality and openness of software and hardware modules makes their construction and maintenance cost high. On the other hand, the parameters of most GB-SAR and GB-MIMO radar systems are difficult to change to adapt to the environment, i.e., the system cannot be easily reconfigured for different applications (for example, the waveform type is fixed and the working frequency is usually in a fixed band). In such a case, the signal processing platform can only passively process the received signal, without the capability to adjust the system parameters in real time according to the obtained results in previous measurements, as needed by cognitive radar [20], [21], the future of modern radar systems. In other word, current GB-SAR and GB-MIMO radar systems have the problem of poor flexibility.

Recently, Software Defined Radar (SDRadar) systems [22]–[24] have been developed to use the Software Defined Radio (SDR) hardware for radar applications, showing the potentials to solve the problems of the complicated, expensive, and non-reconfigurable conventional radar, extending its perspective to educating a wider audience [25] in complement to practical field applications. For different applications, SDRadar only needs to redefine the hardware functions through software programming without the need to change actual hardware device, hence characterized by universality and reconfigurability. Therefore, to reduce the development cost and improve the system flexibility, we demonstrate the use of SDR to implement GBIR systems for displacement estimation in this paper, including an SDR-GB-SAR system to obtain 2D target image and an SDR-GB-MIMO radar system to obtain 3D target image, with different types of commonly used waveforms for displacement measurement by GBIR [1]: stepped fre-

W. F is with Xidian University, Xian, China. J.-M. Friedt is an associate professor at Franche-Comté University with his research activities hosted by the Time & Frequency department of the FEMTO-ST Institute in Besançon, France. E-mail: jmfriedt@femto-st.fr.

quency continuous waveform (SFCW), frequency-modulated continuous waveform (FMCW), and noise waveform (NW). Different from previous approaches [23], [24], this work focuses exclusively on SDRadar running on general purpose central processing unit (CPU) within the free and open-source SDR framework GNU Radio, and does no rely on modifying the Field Programmable Gate Array (FPGA) bit-stream for generating and collecting signals, hence lowering the technical requirements for system development.

Four challenges to realize SDR-GBIR we address in this paper are: 1) synchronization of transmitter and receiver without FPGA programming but keeping the original SDR firmware, 2) using commercial off the shelf (COTS) general SDR hardware to get high range resolution, 3) preprocessing the measured data to reduce the negative influences caused by practical non-ideal factors, and 4) advanced signal processing to obtain high-quality 2D and 3D target image. Specifically, 1) a dual-channel receiver sampling simultaneously the reference signal coupled from the transmitter and the measurement signal collected by the receiving antenna has been applied to system synchronization, 2) the frequency domain bandwidth synthesis approach has been used to obtain high range resolution based on three different waveforms, 3) delay-amplitude calibration and least-squares (LS) based direct-path interference (DPI) suppression [26], [27] have been conducted to improve the system performance, and 4) a novel CS based method have been proposed to improve the imaging quality of SDR-GB-SAR and SDR-GB-MIMO radar systems.

The remainder of this paper is organized as follows. In Section II, the overview of the designed SDR-GBIR system is given, including its structure and working flow, transmitting & receiving (TR) subsystem, and controlling & date acquisition (CDA) subsystem. In Section III, the main signal processing steps, e.g., data preprocessing, high-resolution imaging, and displacement estimation by interferometric process, are introduced. Then, in Section IV, various experiment results are presented to demonstrate the performance of the developed SDR-GBIR systems in practice, together with the displacement estimation accuracy analysis considering atmospheric conditions and the implementation of SDR-GBIR system with orthogonal frequency division multiplexing (OFDM) Wireless Fidelity (Wi-Fi) signal. Finally, section V concludes this paper.

II. System Overview

In this Section, we overview the design method of the SDR-GBIR system, whose general structure is shown in Fig. 1, demonstrating its basic principle and main subsystems. As we can see from Fig. 1, the overall working flow of SDR-GBIR can be expressed as follows:

1) Based on a TCP/IP server written as a Python Module in GNU Radio, the control software (in a personal computer or an embedded single board computer Raspberry Pi 4 – RPi 4) sends commands to GNU Radio through a TCP/IP client;
2) GNU Radio generates and inputs a baseband signal with specific waveform type and parameters to the transmitting unit;
3) After digital to analog conversion (DAC), frequency mixing for up-conversion, power amplifying, and filtering, the RF signal is radiated out by a fixed transmitting antenna in the SDR-GB-SAR case or a selected transmitting antenna in the SDR-GB-MIMO radar case, as well as be coupled to the receiving unit as a reference signal;
4) The receiving unit receives two channels of signals, one being the reference signal from the transmitting unit and the other being the measurement signal collected by a moving or selected receiving antenna;
5) Through filter, low-noise-amplifier, frequency mixer for down-conversion, and analog to digital converter (ADC), the two channels of signals are sampled, interleaved, and transfered continuously by a non-blocking ZeroMQ publish socket;
6) The control software fetches the data through a ZeroMQ subscribe socket and sends it to the Signal Processing (SP) subsystem;
7) Repeat steps 1 to 6 for bandwidth synthesis and antenna moving (or antenna selection);
8) The SP subsystem processes all the received data to obtain target imaging and displacement measurement results and adjusts system parameters accordingly for the following measurements, if needed, by sending commands to the control software.

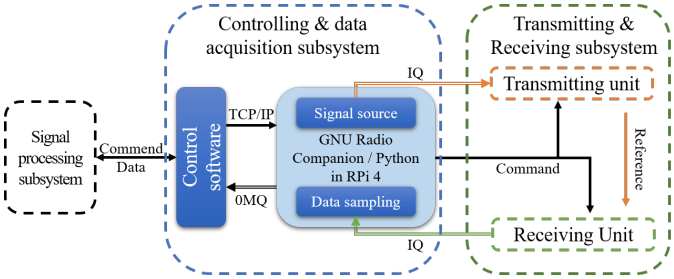

Fig. 1. The general structure of SDR-GBIR with three main subsystems: transmitting & receiving subsystem, controlling & data acquisition subsystem, and signal processing subsystem.

In the following, the functions and components of TR and CDA subsystems will be explained with specific focuses on system synchronization, signal source generation, bandwidth synthesis, parameter changing and data acquisition, leaving details of the SP subsystem and its related signal processing methods in the next Section.

A. Transmitting & receiving subsystem

The first core challenge met by SDRadar implementation is synchronization of the transmitter and the receiver, as general purpose SDR is unable to synchronize emission and reception within sub-microsecond (150 m two-way trip). While the classical approach for synchronization is to modify the FPGA firmware to achieve controlled latency between emission and reception [24], it limits the flexibility of the software approach since the FPGA must be reconfigured for each new emitted sequence. Therefore, we used an approach by separating transmitting and receiving hardware to ease synchronization

issues, as shown in Fig. 2, where a PlutoSDR module from Analog Devices is used as the single-channel transmitter and a USRP B210 from Ettus Research is used as the coherent dual-channel receiver, with one channel (called as reference channel) recording the transmitted signal and the second channel (called as measurement channel) recording the signal collected by the receiving antenna. Under such a scheme, the synchronization between the transmitter and receiver can be obtained for all the applied waveforms, i.e., SFCW, FMCW, and NW, by simple coherent processing methods, as will be explained in the following. The flexibility of this approach is emphasized by replacing the PlutoSDR with a Wi-Fi emitter, proving a covert solution best suited to urban environment monitoring as well as complementing radar application with digital communication, as will be shown in Section IV.

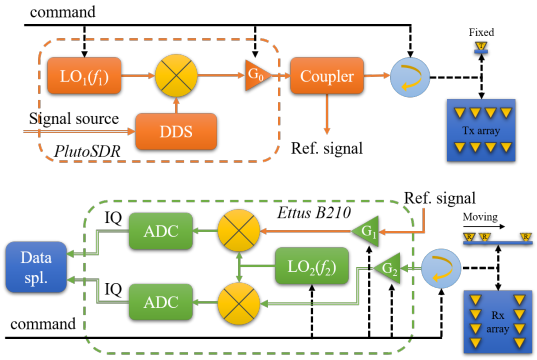

Fig. 2. The transmitting & receiving subsystem of SDR-GBIR: the top sub-figure shows the transmitting unit and the bottom sub-figure shows the receiving unit. DDS refers to Direct Digital Synthesis of the radiofrequency local oscillators LO.

Given the transmitted signal as $s(t) = s_0(t)e^{j(2\pi f_{lo}^1 t+\psi_0)}$ in each TR routine, where $s_0(t)$ is the baseband signal, f_{lo}^1 is the local oscillator frequency of the transmitter, ψ_0 is the initial phase, and t denotes time with a sampling interval of ΔT and a duration of T, the simultaneously sampled reference and measurement signals can be expressed by

$$\begin{cases} s_r(t) = s_0(t-\tau_{ref})e^{j2\pi[\Delta f_{lo}t - f_{lo}^1\tau_{ref}]+j\psi_0} \\ s_m(t) = \sum_{n=1}^{N}\sigma_n s_0(t-\tau_n)e^{j2\pi[\Delta f_{lo}t - f_{lo}^1\tau_n]+j\psi_0} \end{cases} \tag{1}$$

where $\Delta f_{lo} = f_{lo}^1 - f_{lo}^2$ denotes the local oscillator frequency difference, τ_{ref} denotes the delay of the reference channel (a constant value), $\tau_n = \tau_{meas} + \tau_n^0$, $\sigma_n = \sigma_{meas}\sigma_n^0$, τ_{meas} and σ_{meas} denote the intrinsic delay and complex amplitude of the measurement channel caused by the connection cables and other factors (both are a constant value for SDR-GB-SAR or a list of constant values for SDR-GB-MIMO radar), τ_n^0 and σ_n^0 denote the delay and amplitude of the n-th target, and N denotes the number of targets. In Eq. (1), we set the amplitude of the reference channel as 1 without loss of generality.

Since range compression and bandwidth synthesis are conducted in the frequency domain in this study, we obtain the spectrum of the reference and measurement signals as

$$\begin{cases} S_r(f) = S_0(f-\Delta f_{lo})e^{j\psi_0}e^{-j2\pi(f+f_{lo}^2)\tau_{ref}} \\ S_m(f) = S_0(f-\Delta f_{lo})e^{j\psi_0}\sum_{n=1}^{N}\sigma_n e^{-j2\pi(f+f_{lo}^2)\tau_n} \end{cases} \tag{2}$$

where $S_0(f)$ denotes the spectrum of the baseband signal.

Then, combing two channels either by matched filtering or inverse filtering [28], we get a complex signal for range compression as

$$\begin{aligned} S(f) &= S_m(f)S_r^*(f) \\ &= |S_0(f-\Delta f_{lo})|^2\sum_{n=1}^{N}\sigma_n e^{-j2\pi(f+f_{lo}^2)(\tau_n-\tau_{ref})} \end{aligned} \tag{3}$$

with $(\cdot)^*$ as the complex conjugate or

$$\begin{aligned} S(f) &= S_m(f)/S_r(f) \\ &= rc\left(\frac{f-\Delta f_{lo}}{B_0}\right)\sum_{n=1}^{N}\sigma_n e^{-j2\pi(f+f_{lo}^2)(\tau_n-\tau_{ref})} \end{aligned} \tag{4}$$

where $rc(x) = \begin{cases} 1, & -1/2 \le x \le 1/2 \\ 0, & \text{otherwise} \end{cases}$ and B_0 denotes the bandwidth of the baseband signal.

We note that, based on either Eq. (3) or (4), range compression and bandwidth synthesis can be conducted. However, in the former case, the square of spectrum magnitude magnifies any divergence from the flat spectrum, while, in the latter case, such magnitude fluctuation is canceled. Therefore, with a pure reference signal to minimize the signal to noise ratio loss of the inverse filtering method [28], we use Eq. (4) for target imaging and displacement estimation in this study.

It can be seen from Eq. (4) that, by selecting $S_u(f)$ from $S(f)$ with the frequencies satisfying $-B_u/2 \le f_u \le B_u/2$ (where $B_u \le B_0$ denotes the usable bandwidth determined by the maximal possible frequency shift between the local oscillators, as well as the attenuation factor introduced by the filters of the transmitter and receiver), the local oscillator frequency difference Δf_{lo} will not affect the system synchronization, leaving only the constant delay difference $\tau_{meas} - \tau_{ref}$ and the constant complex amplitude σ_{meas}, which, however, can be compensated for in the calibration step. In other word, since the common-clocked reference and measurement channels are both affected by the same frequency offset between transmitter and receiver, computing the complex conjugate product or the direct inversion of one spectrum with the other cancels this effect as long as this frequency offset remains small with respect to the recorded bandwidth, helping the SDR-GBIR system to be synchronized.

For example, as to the SFCW signal, only a single-frequency signal will be transmitted in each TR routine, i.e., $s(t) = e^{j(2\pi f_{lo}^1 t+\psi_0)}$ (assuming its amplitude is constantly one without loss of generality, i.e., $s_0(t) \triangleq 1$). Then, by selecting the maximum of Eq. (4), we get

$$S(\Delta f_{lo}) = \sum_{n=1}^{N}\sigma_n e^{-j2\pi f_{lo}^1(\tau_n-\tau_{ref})} \tag{5}$$

which is not related to Δf_{lo} and contains all the necessary information for the following process. Therefore, it can be concluded that the used approach is suitable for SDR-GBIR system synchronization.

Besides, as shown in Fig. 2, in addition to the single-channel transmitter PlutoSDR and the dual-channel receiver B210, the TR subsystem also includes a transmitting antenna (array) and a receiving antenna (array). In the case of SDR-GB-SAR, a receiving patch antenna is scanning uniformly along a linear rail connected to a micro-controller to achieve the azimuth resolution with a transmitting patch antenna at a fixed location. As to SDR-GB-MIMO radar, small-size, high-gain, and ultra-wideband Vivaldi antennas with the double-slot structure [29] are used to generate the 2D transmitting and receiving arrays, whose corresponding virtual array is a uniform planar array (UPA), to get the azimuth and elevation resolutions. Moreover, for SDR-GB-MIMO radar, two 1×8 switches are added to realize the time-divided signal transmitting and receiving.

B. Controlling & data acquisition subsystem

The CDA subsystem is the main part of software programming for the SDR-GBIR system, which is realized based on an external control software and a single board computer RPi 4, as shown in Fig. 3. Our implementation of the external control software in this paper is with GNU/Octave and its `zeromq` & `socket` toolboxes since digital signal processing can be easily implemented in this framework in a personal computer, although all functions can be ported to Python in order to achieve a fully autonomous implementation running on RPi 4. The consistent embedded GNU/Linux generation framework Buildroot was used in order to provide efficient cross-compilation toolchain, Linux kernel, bootloader, and userspace libraries and applications tuned to the RPi 4 processor characteristics, including GNU Radio Companion, `libuhd` the Universal Hardware Driver for Ettus Research platforms supporting the dual-channel receiver B210 connected to the USB-3 communication bus, `gr-iio` and `libiio` Analog Device's Industrial Input/Output libraries and GNU Radio interface for controlling their hardware for sending data to the transmitter PlutoSDR connected to the USB-2 communication bus, and `numpy` for signal processing with Python3. Such an optimized, custom toolchain is mandatory to achieve best performances of the embedded board which would not be efficiently used with a general purpose, binary distribution [30]: this work contributes by having ported the GNU Radio tools and associated libraries as part of the standard Buildroot packages.

(1) Signal source generation and bandwidth synthesis

The second core challenge met by SDRadar implementation, beyond the system synchronization, is to achieve a wide enough bandwidth to reach a targeted range resolution. However, general SDR hardware (i.e., PlutoSDR and B210) is plagued with the bandwidth limited by the ADC and DAC loss of resolution with increasing sampling rate, as well as the communication bandwidth between SDR and the data acquisition platform (RPi 4), resulting in a poor range resolution. For example, a 2 MHz bandwidth, as provided by

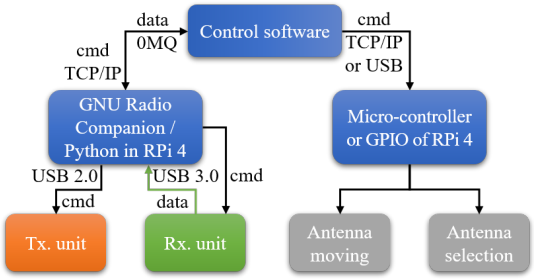

Fig. 3. The controlling & data acquisition subsystem of SDR-GBIR used to control the transmitting parameters, receiving parameters, and antenna moving (or selection), and to send data to and receive commands from the SP subsystem.

the USB-2 communication when sending the baseband signal to PlutoSDR, will only allow for a 75 m range resolution, while, for GBIR displacement estimation, the needed range resolution is normally in meter or sub-meter level [1]. We have observed that no radiofrequency sample was lost when communicating with the PlutoSDR over the USB-2 bus at a sampling rate of 2.7 MS/s, and this sampling rate was hence selected throughout all experiments.

A natural solution to get a wide bandwidth for SDRadar is using the bandwidth synthesis approach [31], and the simplest way is to transmit a single-frequency continuous waveform in each TR routine and increase its carrier frequency step by step until a desired bandwidth, which eventually forms the SFCW signal. Via this method, as can be derived from Eq. (5), we can get a signal vector for range compression as

$$\boldsymbol{s} = [S(\Delta f_{lo}^1), S(\Delta f_{lo}^2), ..., S(\Delta f_{lo}^Q)]^T \tag{6}$$

with $\Delta f_{lo}^q = f_{lo}^{1,q} - f_{lo}^{2,q}$ and

$$\boldsymbol{s}_q = S(\Delta f_{lo}^q) = \sum_{n=1}^{N} \sigma_n e^{-j2\pi f_{lo}^{1,q}(\tau_n - \tau_{ref})} \tag{7}$$

where $(\cdot)^T$ denotes matrix transpose, $q = 1, 2, ..., Q$, Q is the number of frequencies, $f_{lo}^{1,q}$ and $f_{lo}^{2,q}$ denote the q-th local oscillator frequencies of the transmitter and receiver, and $\Delta f_{lo}^{q+1} - \Delta f_{lo}^q = \Delta f$ with Δf as the constant frequency step.

According to Eq.(6), the amplitude and delay of each target can be estimated by the inverse fast Fourier transform (IFFT), resulting in the following high-resolution range profile

$$r(\tau) = \sum_{n=1}^{N} \sigma_n e^{-j2\pi f_c(\tau_n - \tau_{ref})} \frac{\sin[\pi B(\tau - \tau_n + \tau_{ref})]}{\sin[\pi B(\tau - \tau_n + \tau_{ref})/Q]} \tag{8}$$

where $f_c = f_{lo}^{1,1} + (Q-1)\Delta f/2$ denotes the center frequency and $B = Q\Delta f$ denotes the bandwidth of the SFCW signal whose range resolution is thus given by $\delta r = c/2B$, where c denotes the speed of light.

For SFCW signal, the maximal detection range is determined by $r_d = c/(2\Delta f)$. In order to have a larger detection range while keeping the same range resolution, the frequency step should be reduced and thus the number of frequencies

should be increased, resulting in a longer measurement duration. To solve this problem, either the frequency-modulated approach or the phase-coded approach [32], [33] can be applied to each TR routine to fully use the limited bandwidth of SDR. In such a case, as to the q-th TR routine, instead of a single-frequency signal, the transmitted signal can be changed to

$$s_q(t) = e^{-j\pi\gamma(t-T/2)^2} e^{-j(2\pi f_{lo}^{1,q} t + \psi_0^q)} \tag{9}$$

for the frequency-modulated signal with γ as the chirp rate and ψ_0^q as the q-th initial phase, or

$$s_q(t) = \sum_{k=1}^{K} b_k(t) e^{-j\psi_k} e^{-j(2\pi f_{lo}^{1,q} t + \psi_0^q)} \tag{10}$$

for the phase-coded signal with

$$b_k(t) = \begin{cases} 1, & (k-1)\tau_c \le t \le k\tau_c \\ 0, & \text{otherwise} \end{cases} \tag{11}$$

where $k = 1, 2, ..., K$, K is the code length, $\tau_c = T/K$ is the chip interval, and ψ_k denotes the k-th phase value that offsets the relative carrier phase during τ_c [33]. Under the bi-phase coding scheme used in this paper, ψ_k is either 0 or π according to a pseudo-random noise sequence.

In each TR routine, the transmitted signal bandwidth is given by $B_0 = \gamma T$ for the frequency-modulated signal or $B_0 = 1/\tau_c$ for the phase-coded signal, which satisfies $B_0 \le f_s$, where $f_s = 1/\Delta T$ is the data sampling rate. Then, according to Eq. (4), by selecting $S_u(f)$ from $S(f)$ with the frequencies satisfying $-B_0/2 \le -B_u/2 \le f_u \le B_u/2 \le B_0/2$, as presented in sub-Section A, we get the following signal vector in the q-th TR routine

$$\boldsymbol{s}_u^q = [S^q(-B_u/2), S^q(-B_u/2 + \delta f), ..., S^q(B_u/2 - \delta f)]^T \tag{12}$$

where $\delta f = 1/T$, S^q is derived from Eq. (4) correspondingly to the q-th carrier frequency, and the p-th element of $\boldsymbol{s}_u^q$ can be expressed as

$$\boldsymbol{s}_u^{q,p} = \sum_{n=1}^{N} \sigma_n e^{-j2\pi(-B_u/2 + (p-1)\delta f + f_{lo}^{2,q})(\tau_n - \tau_{ref})} \tag{13}$$

where $p = 1, 2, ..., P$, $P = B_u T$ denotes the number of selected frequencies from S^q, and, without loss of generality, P is defined as an even number in the above derivations.

It should be noted that, different from Eq. (7) whose phase term is dependent on the known $f_{lo}^{1,q}$, the phase term in Eq. (13) is dependent on the known $f_{lo}^{2,q}$ and B_u as no maximum selection can be conducted in such a case. Then, by setting the frequency step as $\Delta f = B_u$, we can get a signal vector for range compression as follows

$$\boldsymbol{s} = [(\boldsymbol{s}_u^1)^T, (\boldsymbol{s}_u^2)^T, ..., (\boldsymbol{s}_u^Q)^T]^T \tag{14}$$

At last, the high-resolution range profile can be obtained as

$$r(\tau) = \sum_{n=1}^{N} \sigma_n e^{-j2\pi f_c(\tau_n - \tau_{ref})} \frac{\sin[\pi B(\tau - \tau_n + \tau_{ref})]}{\sin[\pi B(\tau - \tau_n + \tau_{ref})/O]} \tag{15}$$

where $f_c = f_{lo}^{2,1} - B_u/2 + (O-1)\delta f/2$ denotes the center frequency, $O = PQ$, and $B = O\delta f$ denotes the signal bandwidth. Therefore, with $O\delta f = Q\Delta f$, it can be derived that, although the range resolution and the measurement duration are the same, the maximal detection range is increased to $r_d = Pc/(2\Delta f)$, i.e., P times larger than the SFCW signal.

We note that, to make it consistent with the common GBIR statements, we refer the transmitting signals based on Eq. (9) and Eq. (10) with a pseudo-random noise sequence to FMCW and NW, respectively. Besides, a careful decision should be made by minimizing Q since radio-frequency front-end reconfiguration is a time consuming process and hence maximizing B_u within the limitations of the SDR bandwidth and the communication bandwidth. In the case of the USB-2 bus communicating with the PlutoSDR, we have observed that continuous streaming is achieved up to $2 \sim 3$ MS/s.

To summarize, our solution for improving range resolution is adjacent spectra aggregation to synthesize a wider bandwidth, as each narrow-band spectrum is acquired individually before accumulating information in multiple spectral bands to increase the global system bandwidth, a technique also known as "frequency stacking" [24]. In actual SDR-GBIR implementation, we can generate a constant source input, use a Voltage Controlled Oscillator (VCO) block to generate a linearly frequency modulated signal input, and use a Random Source block to generate a pseudo-random phase-coded noise signal input, from GNU Radio, to PlutoSDR for SFCW, FMCW, and NW signal transmitting. Then, by simultaneously sweeping the local oscillator frequencies of PlutoSDR and B210, we can get the desired range resolution. While the default configuration of PlutoSDR is to fully reconfigure the AD9363 radio-frequency front-end with multiple calibration steps requiring up to 1-s to stabilize, custom software was back-ported in the gr-iio library to only reconfigure the local oscillator [34]. Thanks to this configuration, negligible settling time is observed after tuning the PlutoSDR local oscillator. The approach to properly change the local oscillator frequency will be detailed in the following.

(2) Parameter changing and data acquisition

Since the local oscillators of both the transmitter and receiver should be adjusted simultaneously and only when stabilized can relevant data be collected, advanced parameter changing and data acquisition approach should be used as GNU Radio does not allow for discontinuous data-streams to be recorded. The proposed approach, as shown in Fig. 4, is to use a TCP server running in the GNU Radio flowchart to change the local oscillator frequencies under external controlling commands, and to stream collected data to the external control software through a non-blocking UDP-like socket implemented as a ZeroMQ publish socket, as detailed as follows.

Rather than modifying the Python code generated by GNU

Radio, which prevents returning to the graphical user interface once the Python code has been appended with new functionalities, we use the Python Module to add our custom code – namely a separate thread running a TCP server that is able to access the methods provided by the calling program – and execute this thread from the main program by appending the initialization function with the thread call. Calling the thread with the `self` argument allows to modify asynchronously the flow-graph properties and the variables defining the system parameters (e.g., local oscillator frequencies, data sampling rate and duration, signal source type and parameters, TR gains and filtering parameters).

Having found the ability to change the system parameters during a measurement, we should save data when acquisition conditions are stable. Because the continuous data-stream includes the state transition as the hardware properties are modified, the external software controlling the hardware can also synchronize acquisition by fetching the broadcast data only when the hardware is known to be in a stable condition. Rather than using the UDP Sink from GNU Radio, we have selected to use the higher level ZeroMQ framework and its equivalent Publish server. A Subscribe client connects to this server whenever the data-stream is expected to be stable following hardware reconfiguration, and data are otherwise lost if no listening socket has been connected to the server. Since ZeroMQ has been ported to multiple languages, all are suitable for running the client, we have selected GNU/Octave (running on a personal computer) or Python (running on RPi 4 for a fully autonomous implementation) for fetching data. Notice that the flowchart in Fig. 4 does not involve any graphical user interaction and hence is well suited to run on the embedded board, even if lacking a frame buffer or other graphical interfaces.

At last, as shown in Fig. 3, the CDA subsystem also has the functions of moving the receiving antenna on a rail for the SDR-GB-SAR case and selecting the TR antennas for the SDR-GB-MIMO radar case. In the former case, this is achieved by setting the receiving antenna on a motorized rail driven by a lead-screw setup using a stepper motor, controlled by a dedicated micro-controller receiving the commands through its USB (virtual serial) port from the external software controller. In the later case, the two 1×8 switches are connected to the GPIO interface of RPi 4 with a 74LS373 chip as the address latching unit. By changing the voltage levels of the GPIO interface according to the commands from the external software controller, the function of antenna selection is realized.

III. Signal Processing

In this Section, we introduce the details of the SP subsystem, i.e., present the signal processing methods of SDR-GBIR to get high-quality target imaging and displacement estimation results, including data preprocessing, high-resolution imaging, and interferometric process.

A. Data preprocessing

Practical non-ideal factors, especially the DPI caused by the mutual coupling between the transmitting antenna and receiving antenna and the delay-amplitude difference among different measurement channels, may introduce seriously negative effects on the system performance of SDR-GBIR. Therefore, data preprocessing is important to get rid of these influences before target imaging and displacement measurement.

Assuming the transmitting antenna is at its i-th position and the receiving antenna is at its j-th position, where $i = 1, 2, ..., I$ ($I = 1$ for SDR-GB-SAR) and $j = 1, 2, ..., J$, then the practical received reference signal and measurement signal at the q-th carrier frequency can be expressed as

$$\begin{cases} s_r^{i,j,q}(t) = s_0(t-\tau_{ref})e^{j2\pi[\Delta f_{lo}^q t - f_{lo}^{1,q}\tau_{ref}]+j\psi_0^{i,j,q}} \\ s_m^{i,j,q}(t) = s_{m,D}^{i,j,q}(t)+s_{m,T}^{i,j,q}(t)+s_{m,E}^{i,j,q}(t) \end{cases} \tag{16}$$

where

$$s_{m,D}^{i,j,q}(t) = \sigma_D^{i,j,q} s_0(t-\tau_D^{i,j})e^{j2\pi[\Delta f_{lo}^q t - f_{lo}^{1,q}\tau_D^{i,j}]+j\psi_0^{i,j,q}} \tag{17}$$

denotes the DPI component in the measurement channel with $\tau_D^{i,j}$ and $\sigma_D^{i,j,q}$ as its delay and complex amplitude,

$$s_{m,T}^{i,j,q}(t) = \sum_{n=1}^{N} \sigma_n^{i,j,q} s_0(t-\tau_n^{i,j})e^{j2\pi[\Delta f_{lo}^q t - f_{lo}^{1,q}\tau_n^{i,j}]+j\varphi_0^{i,j,q}} \tag{18}$$

denotes the target component in the measurement channel with $\tau_n^{i,j}$ and $\sigma_n^{i,j,q}$ as the delay and complex amplitude of the n-th target component, and $s_{m,E}^{i,j,q}(t)$ denotes the noise component.

The delays and complex amplitudes of the DPI component and the n-th target component can be expressed as

$$\begin{cases} \tau_D^{i,j} = \tau_{meas}^{i,j} + \tau_{D,0}^{i,j}, \quad \tau_n^{i,j} = \tau_{meas}^{i,j} + \tau_{n,0}^{i,j} \\ \sigma_D^{i,j,q} = \sigma_{meas}^{i,j,q}\sigma_{D,0}^{i,j}, \quad \sigma_n^{i,j,q} = \sigma_{meas}^{i,j,q}\sigma_n^0 \end{cases} \tag{19}$$

where $\tau_{meas}^{i,j}$ and $\sigma_{meas}^{i,j,q}$ denote the intrinsic delay and amplitude of the measurement channel caused by the connection cables and other factors (in the SDR-GB-SAR case, they are not dependent on i and j, while, in the SDR-GB-MIMO radar case, they are), $\tau_{D,0}^{i,j}$ and $\tau_{n,0}^{i,j}$ denote the delays of the DPI and the n-the target, $\sigma_{D,0}^{i,j}$ and σ_n^0 denote the amplitudes of the DPI and the n-the target.

In Eqs. (16) and (19), we have the following assumptions: 1) the amplitude of the reference channel is 1; 2) the delays are not related to the frequency; 3) the amplitudes of the DPI is not related to the frequency but related to the antenna position; and 4) the amplitude of the target is neither related to the frequency nor related to the antenna position as the targets are normally at the far range. Besides, we note that, different from Eqs. (1), (7), and (13), which are only used to demonstrate the principles of system synchronization and bandwidth synthesis, here we set the intrinsic amplitude of the measurement channel to be dependent on the frequency, in order to be more consistent with the practice.

For SDR-GB-SAR, with proper setup (e.g., using the similar connection cables for the reference and measurement channels and physically isolating the TR antennas or setting one antenna at the null radiation direction of the other), we have $\tau_{meas}^{i,j} \triangleq$

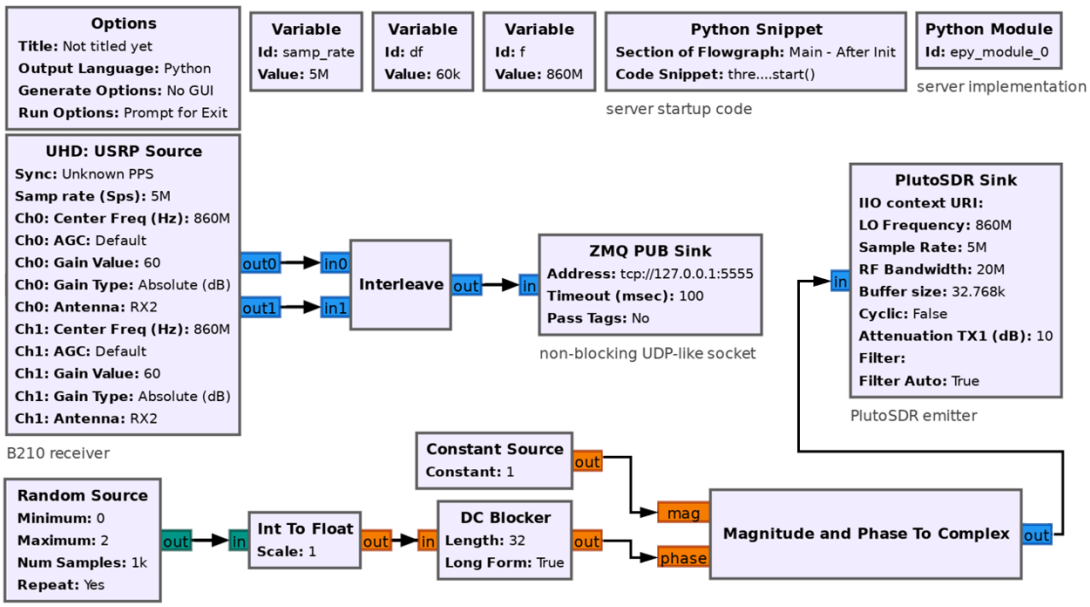

Fig. 4. Demonstration of the inclusion of a TCP server in the Python Module as part of a GNU Radio flow-graph for parameter changing and a non-blocking ZeroMQ publish socket for data acquisition.

$\tau_{meas} \approx \tau_{ref}$, $\sigma_{meas}^{i,j,q} \triangleq \sigma_{meas}^{q} \approx \sigma_{ref}^{q}$, and $\sigma_{D,0}^{i,j,q} \approx 0$. Then, the intrinsic delay-amplitude of the measurement channel and the DPI component will have relatively small impacts on the following process. However, these tricks cannot be used for highly accurate measurements. Besides, for SDR-GB-MIMO radar, the two 1×8 switches will introduce different delays and amplitudes for different channels, and closely-located TR antennas will introduce significant DPIs even in the condition of normal physical isolation. Therefore, some processing methods are needed to compensate for the delay-amplitude difference among different channels and to suppress the DPI. In the following, we use the SFCW signal as an example to explain how can we achieve the delay-amplitude compensated and DPI suppressed signal.

Firstly, by connecting the transmitting and receiving channels through an attenuator directly, we can get the following calibration signal as

$$s_c^{i,j,q}(t) = \sigma_c^{i,j,q} s_0(t - \tau_c^{i,j}) e^{j2\pi[\Delta f_{lo}^q t - f_{lo}^{1,q}\tau_c^{i,j}] + j\psi_0^{i,j,q}} \tag{20}$$

where $\sigma_c^{i,j,q} \approx F\sigma_{meas}^{i,j,q}$ with F as the constant attenuation coefficient and $\tau_c^{i,j} \approx \tau_{meas}^{i,j}$.

Then, by transforming all the signals to the frequency domain, we get

$$\begin{cases} S_r^{i,j,q}(f) = S_0(f - \Delta f_{lo}^q) e^{j\psi_0^{i,j,q}} e^{-j2\pi(f + f_{lo}^{2,q})\tau_{ref}} \\ S_c^{i,j,q}(f) = S_0(f - \Delta f_{lo}^q) e^{j\psi_0^{i,j,q}} \sigma_c^{i,j,q} e^{-j2\pi(f + f_{lo}^{2,q})\tau_c^{i,j}} \\ S_{m,D}^{i,j,q}(f) = S_0(f - \Delta f_{lo}^q) e^{j\psi_0^{i,j,q}} \sigma_D^{i,j,q} e^{-j2\pi(f + f_{lo}^{2,q})\tau_D^{i,j}} \\ S_{m,n}^{i,j,q}(f) = S_0(f - \Delta f_{lo}^q) e^{j\psi_0^{i,j,q}} \sigma_n^{i,j,q} e^{-j2\pi(f + f_{lo}^{2,q})\tau_n^{i,j}} \end{cases} \tag{21}$$

Based on Eq. (21), we can get the signal vectors $\boldsymbol{s}_c^{i,j} \in C^{Q\times 1}$ and $\boldsymbol{s}_m^{i,j} = \boldsymbol{s}_{m,D}^{i,j} + \boldsymbol{s}_{m,T}^{i,j} + \boldsymbol{s}_{m,E}^{i,j} \in C^{Q\times 1}$, whose q-th element can be expressed as

$$\begin{cases} \boldsymbol{s}_C^{i,j}(q) = S_c^{i,j,q}(\Delta f_{lo}^q)/S_r^{i,j,q}(\Delta f_{lo}^q) \\ \quad = \sigma_c^{i,j,q} e^{-j2\pi f_{lo}^{1,q}(\tau_c^{i,j} - \tau_{ref})} \\ \boldsymbol{s}_{m,D}^{i,j}(q) = S_{m,D}^{i,j,q}(\Delta f_{lo}^q)/S_r^{i,j,q}(\Delta f_{lo}^q) \\ \quad = \sigma_D^{i,j,q} e^{-j2\pi f_{lo}^{1,q}(\tau_D^{i,j} - \tau_{ref})} \\ \boldsymbol{s}_{m,T}^{i,j}(q) = S_{m,T}^{i,j,q}(\Delta f_{lo}^q)/S_r^{i,j,q}(\Delta f_{lo}^q) \\ \quad = \sum_{n=1}^{N} \sigma_n^{i,j,q} e^{-j2\pi f_{lo}^{1,q}(\tau_n^{i,j} - \tau_{ref})} \end{cases} \tag{22}$$

Therefore, the following relationships can be satisfied

$$\begin{cases} s_{m,D}^{i,j}(q)/s_C^{i,j}(q) = \sigma_{D,0}^{i,j}/F e^{-j2\pi f_{lo}^{1,q}\tau_{D,0}^{i,j}} \\ s_{m,T}^{i,j}(q)/s_C^{i,j}(q) = \frac{1}{F}\sum_{n=1}^{N} \sigma_n^0 e^{-j2\pi f_{lo}^{1,q}\tau_{n,0}^{i,j}} \end{cases} \tag{23}$$

According to Eq. (23) and considering it is much more significant than the target and noise components, the DPI component in $\boldsymbol{s}_c^{i,j}$ can be suppressed by the LS based method [26], [27] as

$$\widetilde{\boldsymbol{s}}_m^{i,j} = \boldsymbol{s}_m^{i,j} - \boldsymbol{G}(\boldsymbol{G}^H\boldsymbol{G})^{-1}\boldsymbol{G}^H\boldsymbol{s}_m^{i,j} \tag{24}$$

where $(\cdot)^H$ denotes matrix conjugate transpose, $(\cdot)^{-1}$ denotes matrix inverse, and $\boldsymbol{G} \in C^{Q\times L}$ is constructed by the delayed copies of $\boldsymbol{s}_C^{i,j}$ in the frequency domain, given by

$$\boldsymbol{G} = [(\boldsymbol{s}_C^{i,j} \odot e^{-j2\pi \boldsymbol{f}\tau_1}), (\boldsymbol{s}_C^{i,j} \odot e^{-j2\pi \boldsymbol{f}\tau_2}), ..., (\boldsymbol{s}_C^{i,j} \odot e^{-j2\pi \boldsymbol{f}\tau_L})] \tag{25}$$

with $\odot$ as the Hadamard product, $\boldsymbol{f} = [f_{lo}^{1,1}, f_{lo}^{1,2}, ..., f_{lo}^{1,Q}]^T$, and $[\tau_1, \tau_2, ..., \tau_L]$ as the discrete time delays used to properly model the DPI.

At last, the delay-amplitude compensated and DPI suppressed signal vector for the following imaging process and displacement measurement can be obtained by

$$\boldsymbol{s}^{i,j} = \widetilde{\boldsymbol{s}}_m^{i,j}/\boldsymbol{s}_C^{i,j} \approx \frac{1}{F}\sum_{n=1}^{N}\sigma_n^0 e^{-j2\pi \boldsymbol{f}\tau_{n,0}^{i,j}} + \boldsymbol{s}_E^{i,j} \tag{26}$$

Actually, an alternative approach based on atomic norm minimization and Vandermonde decomposition [26] can be used for DPI suppression after delay-amplitude compensation. In such a case, we first get the DPI-included but delay-amplitude compensated signal vector as

$$\boldsymbol{s}_0^{i,j} = \boldsymbol{s}_m^{i,j}/\boldsymbol{s}_C^{i,j} = \boldsymbol{s}_D^{i,j} + \boldsymbol{s}_T^{i,j} + \boldsymbol{s}_E^{i,j} \tag{27}$$

where $\boldsymbol{s}_D^{i,j} = \sigma_{D,0}^{i,j}/F e^{-j2\pi \boldsymbol{f}\tau_{D,0}^{i,j}}$. Then, by formulating Eq. (27) as a 1D frequency estimation problem, the DPI component in $\boldsymbol{s}_0^{i,j}$ can be estimated by solving

$$\begin{aligned} &[\widetilde{\boldsymbol{s}}_D^{i,j}, \widetilde{\boldsymbol{u}}] = \min_{\boldsymbol{s}_D^{i,j}, \boldsymbol{u}} \operatorname{trace}[T(\boldsymbol{u})] \\ &s.t. \begin{bmatrix} 1 & (\boldsymbol{s}_D^{i,j})^H \\ \boldsymbol{s}_D^{i,j} & T(\boldsymbol{u}) \end{bmatrix} \geq 0, ||\boldsymbol{s}_0^{i,j} - \boldsymbol{s}_D^{i,j}||_2^2 \leq \varepsilon_n \end{aligned} \tag{28}$$

where $\operatorname{trace}[\cdot]$ denotes the trace of a matrix, $T(\boldsymbol{u})$ denotes a Toeplitz matrix formed by the vector $\boldsymbol{u}$, and ε_n denotes the target plus noise power level.

After solving Eq. (28) and conducting Vandermonde decomposition and LS based amplitude estimation to get the DPI approximation $\widetilde{\boldsymbol{s}}_D^{i,j}$, the DPI component in $\boldsymbol{s}_0^{i,j}$ can be suppressed, giving us

$$\boldsymbol{s}^{i,j} = \boldsymbol{s}_0^{i,j} - \widetilde{\boldsymbol{s}}_D^{i,j} \approx \frac{1}{F}\sum_{n=1}^{N}\sigma_n^0 e^{-j2\pi \boldsymbol{f}\tau_{n,0}^{i,j}} + \boldsymbol{s}_E^{i,j} \tag{29}$$

We note that, in comparison with the method in Eq. (26), the method in Eq. (29) is more effective but also more time-consuming. Therefore, we used the former method in the experiments, which works well as observed. Besides, the reasons why DPI suppression is not conducted in the time domain are: 1) the intrinsic amplitude of the measurement channel is assumed to be frequency-dependent, hence it is better to be processed in the frequency domain, and 2) the delay of DPI is not exactly integral times of the data sampling interval ΔT, preventing the methods working in the time domain from mitigating the DPI component effectively, considering that a 2-MS/s sampling rate gives a sampling interval of 150 m (one-way) which is much larger than the DPI delay. Furthermore, although the above derivations are conducted based on the SFCW signal, there is no problem when applied to the FMCW and NW signals, as all these three signals have the same type in the frequency domain after inverse filtering.

B. High-resolution imaging

After data preprocessing, high-resolution imaging should be performed to get the focused image of the observation scene to distinguish different targets. For GBIR, back projection algorithm (BPA), range migration algorithm (RMA), and far-field pseudo-polar format algorithm (FPFA) are commonly used [35]–[37]. Compared with other algorithms, BPA is more universal as it can be used without geometric limitations and approximations, hence is selected for SDR-GBIR in this study to not limit its system flexibility. In the following, again, we use the SFCW signal as an example to explain how to obtain a high-quality target image, which can also be applied to the cases with FMCW and NW signals.

Firstly, the signal vector echoed from all the targets in the observation scene measured at all frequencies and antenna positions can be written as

$$\boldsymbol{y} = [(\boldsymbol{s}^{1,1})^T, (\boldsymbol{s}^{1,2})^T, ..., (\boldsymbol{s}^{I,J})^T]^T \in C^{IJQ\times 1} \tag{30}$$

whose $[(i-1)JQ+(j-1)Q+q]$-th element can be expressed as

$$\begin{aligned} \boldsymbol{y}^{i,j,q} &= \iiint_{\Omega} \sigma_{x,y,z} e^{-j2\pi f_q \tau_{x,y,z}^{i,j}} dxdydz + n_{i,j,q} \\ &\approx \sum_{u=1}^{U}\sum_{v=1}^{V}\sum_{w=1}^{W} \sigma_{x_u,y_v,z_w} e^{-j2\pi f_q \tau_{x_u,y_v,z_w}^{i,j}} + n_{i,j,q} \end{aligned} \tag{31}$$

where Ω denotes the observation scene, $n_{i,j,q}$ denotes the noise, U, V, and W denote the numbers of the discretization grids in the x, y, and z directions, σ_{x_u,y_v,z_w} denotes the amplitude of the target at (x_u, y_v, z_w), and $\tau_{x_u,y_v,z_w}^{i,j}$ denotes its delay with respect to the i-th transmitting antenna at (x_i, y_i, z_i) and j-th receiving antenna at (x_j, y_j, z_j), given by

$$\tau_{x_u,y_v,z_w}^{i,j} = [R_{x_u,y_v,z_w}^{i} + R_{x_u,y_v,z_w}^{j}]/c \tag{32}$$

with $R_{x_u,y_v,z_w}^{i} = [(x_i - x_u)^2 + (y_i - y_v)^2 + (z_i - z_w)^2]^{1/2}$ and $R_{x_u,y_v,z_w}^{j} = [(x_j - x_u)^2 + (y_j - y_v)^2 + (z_j - z_w)^2]^{1/2}$.

Then, the signal vector $\boldsymbol{y}$ can be rewritten as

$$\boldsymbol{y} = \boldsymbol{\Phi}\boldsymbol{\sigma} + \boldsymbol{n} \tag{33}$$

with $\boldsymbol{\sigma} = [\sigma_{x_1,y_1,z_1}, \sigma_{x_1,y_1,z_2}, ..., \sigma_{x_U,y_V,z_W}] \in C^{UVW\times 1}$, $\boldsymbol{n} = [n_{1,1,1}, n_{1,1,2}, ..., n_{I,J,Q}] \in C^{IJQ\times 1}$, and

$$\boldsymbol{\Phi} = \begin{bmatrix} e^{-j2\pi \boldsymbol{f}\tau_{x_1,y_1,z_1}^{1,1}} & \cdots & e^{-j2\pi \boldsymbol{f}\tau_{x_U,y_V,z_W}^{1,1}} \\ \vdots & \ddots & \vdots \\ e^{-j2\pi \boldsymbol{f}\tau_{x_1,y_1,z_1}^{I,J}} & \cdots & e^{-j2\pi \boldsymbol{f}\tau_{x_U,y_V,z_W}^{I,J}} \end{bmatrix} \tag{34}$$

By coherently summing the signals at all antenna positions and frequencies, the amplitude of the target at (x_u, y_v, z_w) can be estimated by BPA as

$$\boldsymbol{\sigma}_{x_u,y_v,z_w}^{BP} = \frac{1}{IJQ}\sum_{i=1}^{I}\sum_{j=1}^{J}\sum_{q=1}^{Q} \boldsymbol{y}^{i,j,q} e^{+j2\pi f_q \tau_{x_u,y_v,z_w}^{i,j}} \tag{35}$$

Therefore, the vectorized amplitudes of all targets can be estimated by

$$\boldsymbol{\sigma}^{BP} = \frac{1}{IJQ}\boldsymbol{\Phi}^H \boldsymbol{y} \tag{36}$$

It can be seen from Eq. (36) that the BPA uses $\frac{1}{IJQ}\boldsymbol{\Phi}^H$ to approximate the inverse of $\boldsymbol{\Phi}$ to solve Eq. (33). If the columns of $\boldsymbol{\Phi}$ are orthogonal (or near orthogonal) to each other, i.e., $\frac{1}{IJQ}\boldsymbol{\Phi}^H\boldsymbol{\Phi} \approx \boldsymbol{I}$, where $\boldsymbol{I}$ is the unit matrix, and the targets are located exactly at the discretized grids, Eq. (36) can get a well-focused target image. If the grid size is decreased to more accurately locate the targets, i.e., UVW becomes (much) bigger than IJQ, the columns of $\boldsymbol{\Phi}$ are no longer orthogonal but correlated, resulting in high-level sidelobes in the obtained target image. Sidelobes of strong targets may make the weak targets undetectable and sidelobes of multiple targets produce spurious peaks, resulting in negative effects on the following processing, i.e., displacement estimation in our case. To improve the imaging resolution and avoid sidelobes, a popular approach is to explore the sparsity of $\boldsymbol{\sigma}$ based on the CS theory [3], [38] by solving the minimization problem

$$\boldsymbol{\sigma}^{CS} = \min ||\boldsymbol{\sigma}||_0 \quad s.t.\ ||\boldsymbol{y} - \boldsymbol{\Phi}\boldsymbol{\sigma}||_2 \leq \varepsilon \tag{37}$$

where ε denotes the noise power level.

Normally, to handle the NP-hard task of solving Eq. (37), an appealing approach is to relax the L_0 norm to the L_1 norm, giving the Lasso optimization problem

$$\boldsymbol{\sigma}^{CS} = \min_{\boldsymbol{\sigma}} \frac{1}{2}||\boldsymbol{y} - \boldsymbol{\Phi}\boldsymbol{\sigma}||_2^2 + \lambda||\boldsymbol{\sigma}||_1 \tag{38}$$

where λ is a scalar.

An effective way to solve Eq. (38) is to use the iterative soft thresholding algorithm (ISTA) [39], where the solution at the $[k+1]$-th iteration is given by

$$\boldsymbol{\sigma}_{k+1} = \eta_{\theta_{k+1}}[\boldsymbol{\sigma}_k + \mu_{k+1}\boldsymbol{\Phi}^H(\boldsymbol{y} - \boldsymbol{\Phi}\boldsymbol{\sigma}_k)] \tag{39}$$

with $\eta_{\theta_{k+1}}[x] = x/|x|\max(|x| - \theta_{k+1}, 0)$ as the soft shrinkage function and μ_{k+1} as the step size.

To accelerate the convergence, the fast ISTA (FISTA) is proposed in [40], whose $[k+1]$-th iteration is in the form of

$$\begin{cases} \boldsymbol{\sigma}_{k+1} = \eta_{\theta_{k+1}}[\boldsymbol{\rho}_k + \mu_{k+1}\boldsymbol{\Phi}^H(\boldsymbol{y} - \boldsymbol{\Phi}\boldsymbol{\rho}_k)] \\ \xi_{k+1} = (1 + \sqrt{1 + 4\xi_k^2})/2 \\ \boldsymbol{\rho}_{k+1} = \boldsymbol{\sigma}^{k+1} + \frac{\xi_k - 1}{\xi_{k+1}}(\boldsymbol{\sigma}_{k+1} - \boldsymbol{\sigma}_k) \end{cases} \tag{40}$$

However, with large values of IJQ and UVW, the computational cost and memory usage of Eq. (40) are normally beyond the computing capacity of a general personal computer, making it unsuitable for SDR-GBIR target imaging in practice. Therefore, inspired by the approximated CS based methods [41], [42], we propose a method to solve Eq. (38) effectively, giving an imaging method for SDR-GBIR to get high-resolution target images with low computational cost and small memory usage.

In general, considering that the most time-consuming parts in Eq. (40) are the two matrix-vector multiplications $\boldsymbol{\Phi}^H\boldsymbol{b}_k$ and $\boldsymbol{a}_k = \boldsymbol{\Phi}\boldsymbol{\rho}_k$, where $\boldsymbol{b}_k = \boldsymbol{y} - \boldsymbol{a}_k$, we try to more effectively calculate $\boldsymbol{c}_k = \boldsymbol{\Phi}^H\boldsymbol{b}_k$ and $\boldsymbol{a}_k$ without loading $\boldsymbol{\Phi}$ in each iteration to also save the memory usage. At first, it can be easily deirved that the $[(u-1)VW + (v-1)W + w]$-th element of $\boldsymbol{c}_k$ is actually obtained by

$$\boldsymbol{c}_k^{u,v,w} = \sum_{i=1}^{I}\sum_{j=1}^{J}\sum_{q=1}^{Q} \boldsymbol{b}_k^{i,j,q} e^{+j2\pi f_q \tau_{x_u,y_v,z_w}^{i,j}} \tag{41}$$

where $\boldsymbol{b}_k^{i,j,q}$ denotes the $[(i-1)JQ + (j-1)Q + q]$-th element of $\boldsymbol{b}_k$, similar to the BPA shown in Eq. (35).

Hence, Eq. (41) can be accelerated by using IFFT and sinc interpolation, which is normally applied by the BPA working in the time domain [3], giving

$$\boldsymbol{c}_k^{u,v,w} = \sum_{i=1}^{I}\sum_{j=1}^{J} \mathcal{I}_{\text{sinc}}[\mathcal{F}_{\text{inv}}(\boldsymbol{b}_k^{i,j}, M) \odot \boldsymbol{\alpha}, \tau_{x_u,y_v,z_w}^{i,j}]\boldsymbol{\beta}_{x_u,y_v,z_w}^{i,j} \tag{42}$$

where $\mathcal{F}_{\text{inv}}(\cdot, M)$ denotes IFFT with the length of M (typically a power of 2), $\boldsymbol{\alpha} \in C^{M\times 1}$ with its m-th element as $\boldsymbol{\alpha}_m = e^{-j\pi(m-1)(Q-1)/M}$, $\boldsymbol{\beta}_{u,v,w}^{i,j} = e^{j2\pi f_c \tau_{x_u,y_v,z_w}^{i,j}}$, and $\mathcal{I}_{\text{sinc}}[\cdot, \tau_{x_u,y_v,z_w}^{i,j}]$ denotes the sinc interpolation at $\tau_{x_u,y_v,z_w}^{i,j}$. Therefore, $\boldsymbol{c}_k$ can be obtained by

$$\boldsymbol{c}_k = \sum_{i=1}^{I}\sum_{j=1}^{J} \mathcal{I}_{\text{sinc}}[\mathcal{F}_{\text{inv}}(\boldsymbol{b}_k^{i,j}, M) \odot \boldsymbol{\alpha}, \boldsymbol{\tau}^{i,j}] \odot \boldsymbol{\beta}^{i,j} \tag{43}$$

with $\boldsymbol{\tau}^{i,j} = [\tau_{x_1,y_1,z_1}^{i,j}, \tau_{x_1,y_1,z_2}^{i,j}, ..., \tau_{x_U,y_V,z_W}^{i,j}] \in C^{UVW\times 1}$ and $\boldsymbol{\beta}^{i,j} = [\beta_{1,1,1}^{i,j}, \beta_{1,1,2}^{i,j}, ..., \beta_{U,V,W}^{i,j}] = e^{j2\pi f_c \boldsymbol{\tau}^{i,j}}$.

To be more time-saving, the Type-II non-uniform FFT (NUFFT) with fast Gaussian gridding [43], [44] working with uniform frequencies but non-uniform delays can be employed to replace the IFFT and sinc interpolation, giving

$$\boldsymbol{c}_k = \sum_{i=1}^{I}\sum_{j=1}^{J} \mathcal{N}_{\text{II}}[\boldsymbol{b}_k^{i,j}, 2\pi\Delta f \boldsymbol{\tau}^{i,j}] \odot \boldsymbol{\beta}^{i,j} \tag{44}$$

where $\mathcal{N}_{\text{II}}[FK, XJ]$ denotes the Type-II NUFFT with FK as the input Fourier coefficient values and XJ as the location of output values.

Similarly, it can be derived that the $[(i-1)JQ + (j-1)Q + q]$-th element of $\boldsymbol{a}_k$ is actually obtained by

$$\boldsymbol{a}_k^{i,j,q} = \sum_{u=1}^{U}\sum_{v=1}^{V}\sum_{w=1}^{W} \boldsymbol{\rho}_k^{u,v,w} e^{-j2\pi f_q \tau_{x_u,y_v,z_w}^{i,j}} \tag{45}$$

Therefore, the signal vector $\boldsymbol{a}_k^{i,j} \in C^{Q\times 1}$ with respect to the i-th transmitting antenna and j-th receiving antenna can be obtained by the Type-I NUFFT working with non-uniform delays but uniform frequencies, giving

$$\boldsymbol{a}_k^{i,j} = UVW\mathcal{N}_{\text{I}}[\boldsymbol{\rho}_k \odot (\boldsymbol{\beta}^{i,j})^*, 2\pi\Delta f \boldsymbol{\tau}^{i,j}, Q] \tag{46}$$

where $\mathcal{N}_{\text{I}}[CJ, XJ, MS]$ denotes the Type-I NUFFT with CJ as the strengths of sources, XJ as the location of sources, and MS as the number of output values [43], [44].

Based on Eqs. (44) and (46), we can solve the Lasso optimization problem in Eq. (38) effectively with the FISTA for SDR-GBIR high-resolution and high-quality target imaging. Since it is based on NUFFT and FISTA, we call the

proposed imaging method as NUFFT-FISTA, whose detailed implementation is summarized in Table. I.

Compared to the calculations shown in Eq. (40), since the matrix-vector multiplications are replaced with NUFFTs in the proposed method, there is no need to construct $\boldsymbol{\Phi}$, only $\boldsymbol{\tau}^{i,j}$ with $i = 1, 2, ..., I$ and $j = 1, 2, ..., J$ needs to be saved and loaded, hence significantly reducing the storage cost (from $IJQ \times UVW$ to $IJ \times UVW$). Besides, in each iteration of FISTA, the computational complexity in terms of multiplications is changed from $2IJQUVW$ to $2IJ[(4M_{sp}+1)UVW + Q_r log_2(Q_r)]$ with M_{sp} as the spreading parameter and $Q_r = CQ$, where C is the oversampling ratio [43], [45]. When Q is large, which is normally the case in order to obtain a high range resolution, the computational cost can also be much reduced by the proposed method.

TABLE I
NUFFT-FISTA FOR SDR-GBIR TARGET IMAGING.

Input: $\boldsymbol{y}$, θ, μ, max iteration number K, and stop parameter ς
Initial: $\boldsymbol{\sigma}_0 = 0$, $\boldsymbol{\rho}_0 = 0$, and $\xi_0 = 1$
for $k = 0$ **to** $K - 1$ **do**
  for $i = 1$ **to** I **do**
    for $j = 1$ **to** J **do**
      $\boldsymbol{a}_k^{i,j} = UVW\mathcal{N}_1[\boldsymbol{\rho}_k \odot (\boldsymbol{\beta}^{i,j})^*, 2\pi\Delta f\boldsymbol{\tau}^{i,j}, Q]$
    end for
  end for
  $\boldsymbol{b}_k = \boldsymbol{y} - \boldsymbol{a}_k$
  $\boldsymbol{c}_k = \sum_{i=1}^{I}\sum_{j=1}^{J} \mathcal{N}_{\mathrm{II}}[\boldsymbol{b}_k^{i,j}, 2\pi\Delta f\boldsymbol{\tau}^{i,j}] \odot \boldsymbol{\beta}^{i,j}$
  $\boldsymbol{\sigma}_{k+1} = \eta_{\theta_{k+1}}[\boldsymbol{\rho}_k + \mu_{k+1}\boldsymbol{c}_k]$
  $\xi_{k+1} = (1 + \sqrt{1 + 4\xi_k^2})/2$
  $\boldsymbol{\rho}_{k+1} = \boldsymbol{\sigma}^{k+1} + \frac{\xi_k - 1}{\xi_{k+1}}(\boldsymbol{\sigma}_{k+1} - \boldsymbol{\sigma}_k)$
  if $|\boldsymbol{\sigma}^{k+1} - \boldsymbol{\sigma}^k|_2 / |\boldsymbol{\sigma}^k|_2 < \varsigma$ **then**
    $K_0 = k + 1$
    stop iteration
  end if
end for
Return: $\boldsymbol{\sigma}_{K_0}$ or $\boldsymbol{\sigma}_K$

Beyond high-resolution and low sidelobe level, another advantage of the proposed imaging method lies on the reduction of measurement duration for SDR-GBIR. Based on the CS theory, $\boldsymbol{\sigma}$ can be estimated from Eq. (38) with under-sampled data. Thanks to this, we can reduce the number of frequencies (Q) for bandwidth synthesis and reduce the numbers of antenna positions (I and J) without affecting the performance of SDR-GBIR, hence reduce the measurement duration. In such a case, by randomly selecting $Q_1 \leq Q$ carrier frequencies in a given bandwidth B and selecting $I_1 \leq I$ and $J_1 \leq J$ antenna positions in a given aperture or given TR arrays, we get the optimization problem for SDR-GBIR target imaging as

$$\boldsymbol{\sigma}^{CS} = \min_{\boldsymbol{\sigma}} \frac{1}{2}||\boldsymbol{y}_1 - \boldsymbol{\Phi}_1\boldsymbol{\sigma}||_2^2 + \lambda||\boldsymbol{\sigma}||_1 \tag{47}$$

where $\boldsymbol{y}_1 \in C^{I_1J_1Q_1 \times 1}$ is the under-sampled data after preprocessing (note that the methods for DPI suppression and delay-amplitude compensation shown in Eq. (26) and Eq. (29) can still work well with under-sampled frequencies [26]) and $\boldsymbol{\Phi}_1 \in C^{I_1J_1Q_1 \times UVW}$ is obtained by only selecting the rows of $\boldsymbol{\Phi}$ corresponding to the sampled frequencies and antenna positions with $I_1J_1Q_1 \ll IJQ$.

To solve Eq. (47), a natural approach is to use the same processing flow given in Table. I by making $\boldsymbol{b}_k^{(i,j,q)\in\Gamma} = \boldsymbol{y}_1 - \boldsymbol{a}_k^{(i,j,q)\in\Gamma}$ and $\boldsymbol{b}_k^{(i,j,q)\notin\Gamma} = 0$, where $\Gamma \in R^{I_1J_1Q_1 \times 1}$ is the indexes of selected frequencies and antenna positions [46]. An alternative approach is to use the Type-III NUFFT working with non-uniform inputs and non-uniform outputs to calculate $\boldsymbol{a}_k$ and $\boldsymbol{c}_k$ directly, i.e.,

$$\begin{cases} \boldsymbol{a}_k^{i_1,j_1} = \mathcal{N}_{\mathrm{III}}[\boldsymbol{\rho}_k \odot (\boldsymbol{\beta}_1^{i_1,j_1})^*, 2\pi\boldsymbol{\tau}_1^{i_1,j_1}\Delta f, \frac{\boldsymbol{f}_1 - f_c}{\Delta f}] \\ \boldsymbol{b}_k = \boldsymbol{y}_1 - \boldsymbol{a}_k \\ \boldsymbol{c}_k = \sum_{i_1=1}^{I_1}\sum_{j_1=1}^{J_1} \mathcal{N}_{\mathrm{III}}[\boldsymbol{b}_k^{i_1,j_1}, \frac{2\pi(\boldsymbol{f}_1 - f_c)}{Q\Delta f}, \boldsymbol{\tau}_1^{i_1,j_1}Q\Delta f] \odot \boldsymbol{\beta}_1^{i_1,j_1} \end{cases} \tag{48}$$

where $\mathcal{N}_{\mathrm{III}}[CJ, XJ, SK]$ denotes the Type-III NUFFT with CJ as the strengths of sources, XJ as the location of sources, and SK as the locations of output values, $\boldsymbol{f}_1$ denotes the vector of selected frequencies, $\boldsymbol{\tau}_1$ is obtained from $\boldsymbol{\tau}$ corresponding to the selected antennas, and $\boldsymbol{\beta}_1^{i_1,j_1} = e^{j2\pi f_c \boldsymbol{\tau}_1^{i_1,j_1}}$.

C. Interferometric process

Based on the BPA or the proposed imaging method, a 2D or 3D complex image of the observation scene can be obtained by turning the vectorized complex amplitudes $\boldsymbol{\sigma}$ to a matrix or a tensor. The amplitude of the image can be used to interpret the scattering properties of the observed scene (i.e., to differentiate targets with potential displacements) while the phase of the image can be exploited to measure the target displacement when a temporal baseline is introduced.

Assuming $\boldsymbol{I}_M$ and $\boldsymbol{I}_S$ are the two images obtained at different time, their phase difference can be calculated to generate an interferogram as $\Delta\boldsymbol{\Psi} = \arg[\boldsymbol{I}_S(\boldsymbol{I}_M)^*]$, where $\arg[\cdot]$ denotes the argument of a complex value. Then, to evaluate the quality of the interferogram, a coherence image can be generated [47], whose $[u, v, w]$-th element is given by

$$\Upsilon^{u,v,w} = \frac{\left|E\left\{I_S^{u,v,w}(I_M^{u,v,w})^*\right\}\right|}{\sqrt{E\left\{|I_S^{u,v,w}|^2\right\}E\left\{|I_M^{u,v,w}|^2\right\}}} \tag{49}$$

where $E\{\cdot\}$ denotes the expectation.

In practice, the expectation operation in Eq. (49) is always approximated by a moving average process, i.e.,

$$\widetilde{\Upsilon}^{u,v,w} = \frac{\left|\sum_{l_1}\sum_{l_2}\sum_{l_3} g_S^{l_1,l_2,l_3}(g_M^{l_1,l_2,l_3})^*\right|}{\sqrt{\sum_{l_1}\sum_{l_2}\sum_{l_3}\left|g_S^{l_1,l_2,l_3}\right|^2\left|g_M^{l_1,l_2,l_3}\right|^2}} \tag{50}$$

where $g_S^{l_1,l_2,l_3} = I_S^{u+l_1,v+l_2,w+l_3}$, $g_M^{l_1,l_2,l_3} = I_M^{u+l_1,v+l_2,w+l_3}$, $l_1 \in [-L_1/2, L_1/2]$, $l_2 \in [-L_2/2, L_2/2]$, and $l_3 \in [-L_3/2, L_3/2]$ with $L_1 \times L_2 \times L_3$ as the size of the moving window.

Since GBIR can only get an accurate displacement estimation for the target with a high coherence value (i.e., with a low

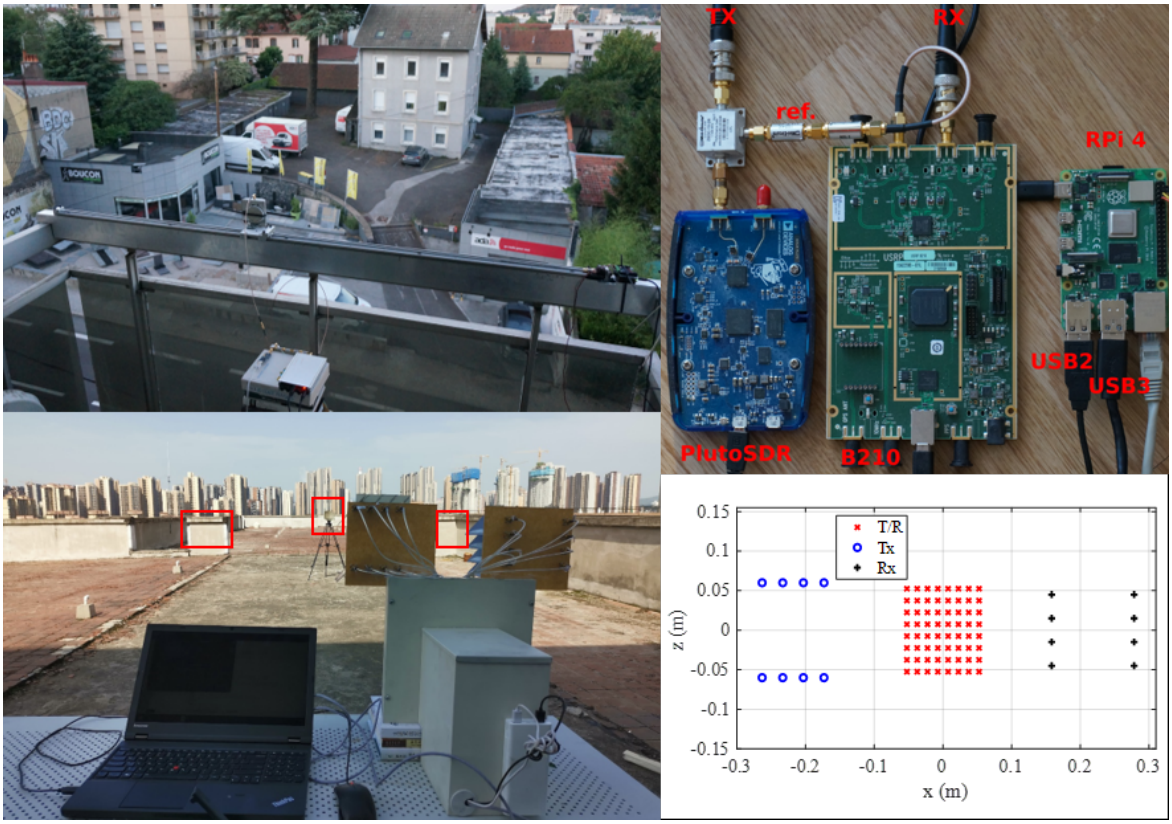

Fig. 5. Experiment setups: the left-top sub-figure corresponds to the SDR-GB-SAR system, the left-bottom sub-figure corresponds to the SDR-GB-MIMO radar system, the right-top sub-figure shows the TR subsystem of both systems, and the right-bottom sub-figure shows the antenna geometry of the SDR-GB-MIMO radar system.

phase noise), target selection is conducted by thresholding the interferogram based on the coherence image, resulting in

$$\Delta\boldsymbol{\Psi}_T = \Delta\boldsymbol{\Psi}_{\boldsymbol{\Upsilon}\geq\Upsilon_T} \tag{51}$$

where Υ_T is a user-defined threshold to balance the interferogram quality and the spatial density of the selected targets.

At last, after phase unwrapping and atmospheric phase compensation (see [1] and the references therein), which give us $\Delta\widetilde{\boldsymbol{\Psi}}_T$, the target displacements along the radar line of sight (LOS) direction can be estimated by

$$\boldsymbol{d}_T = c\Delta\widetilde{\boldsymbol{\Psi}}_T \Big/ (4\pi f_c) \tag{52}$$

IV. Experiment Results

In this Section, we give some experiment results and their interpretation/analysis to show the practical performance of the developed SDR-GBIR systems and to validate the proposed preprocessing and processing methods. The experiment setups of the developed SDR-GB-SAR system and SDR-GB-MIMO radar system are shown in Fig. 5. In general, this Section mainly includes six parts: 1) demonstration of system synchronization; 2) validation of bandwidth synthesis; 3) functions of data preprocessing; 4) target 2D & 3D imaging results; 5) displacement estimation and analysis; and 6) system implementation with Wi-Fi signal.

A. Demonstration of system synchronization

At first, by assessing the phase and delay estimations of the SFCW signal, we demonstrate the synchronization of the transmitter and receiver obtained by the proposed scheme. The experiment has been conducted by directly connecting different transceiver pairs of the SDR-GB-MIMO radar system with changing carrier frequencies from 4.85 GHz to 5.15 GHz. As shown in Eq. (5) with $N = 1$, by selecting the maximum of Eq. (4), we get a complex value whose phase term is dependent on the carrier frequency f_{lo}^1 and the delay difference $\tau_n - \tau_{ref}$. Therefore, the phase terms corresponding to different carrier frequencies should be linearly ascending or descending if the delay difference is a constant. Besides, the single constant delay difference should be able to be accurately estimated by the inverse Fourier transform. If the system has not been well synchronized, the linear phase and single delay constant difference assumptions are not met. The results shown in Fig. 6 fit well to these analysis, demonstrating the system synchronization. The isolation between the reference and measurement receiving channels of the B210 is measured at about 94±2 dB at 600 MHz, 89± dB at 1000 MHz, 60±2 dB at 2400 MHz, 66±2 dB at 5000 MHz and 57±2 dB at 5800 MHz.

B. Validation of bandwidth synthesis

Range resolution improvement obtained by bandwidth synthesis is validated by assessing the SDR-GB-SAR system

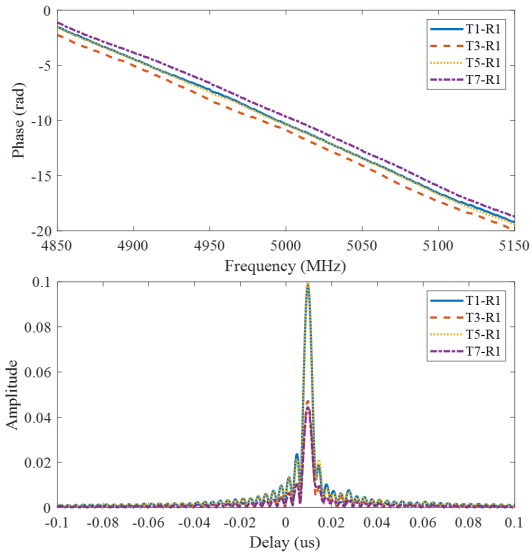

Fig. 6. System synchronization demonstrated by assessing the phase (top) and delay (bottom) estimations for different transceiver pairs of the developed SDR-GB-MIMO radar system.

using the NW signal. The spectra of the random noise based bi-phase-coded signals with four different carrier frequencies are shown in Fig. 7, where the vertical black lines correspond to the carrier frequencies with a step of $\delta f = 1$ MHz. Then, by selecting the frequencies satisfying $-B_u/2 \leq f_u \leq B_u/2$ with $B_u = 1$ MHz from each spectrum, a signal vector can be obtained by Eqs. (12) and (14), giving the range compression results shown in Fig. 8 with $Q = 1, 10, 50$ and 100. It can be seen that, via the bandwidth synthesis approach, the range resolution can be gradually improved along with the increasing number of carrier frequencies, making the reflections of different targets in the scene (tree, car, house, and so on, as shown in the left-top sub-figure of Fig. 5) more and more distinguishable in the range direction.

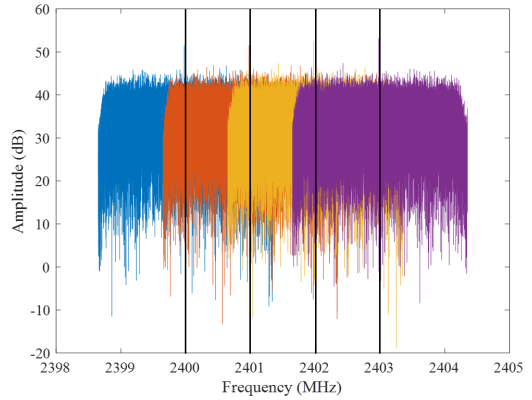

Fig. 7. Spectra of the random noise based bi-phase-coded signals with carrier frequencies of 2400, 2401, 2402, and 2403 MHz.

C. Functions of data preprocessing

With and without DPI suppression and delay-amplitude compensation, the functions of the proposed data preprocessing method are shown by assessing the SDR-GB-MIMO radar system with a trihedral corner reflector (CR) and multiple walls as the targets, as indicated by the red rectangles in the left-bottom sub-figure of Fig. 5. With transmitter-1/receiver-1 and transmitter-1/receiver-2, the range compression results are shown in Fig. 9 and Fig. 10, respectively.

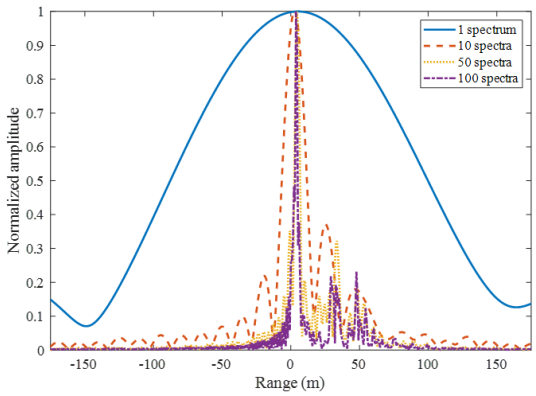

Fig. 8. Range compression results of the developed SDR-GB-SAR system obtained by synthesizing $Q = 1, 10, 50$ and 100 NW spectra.

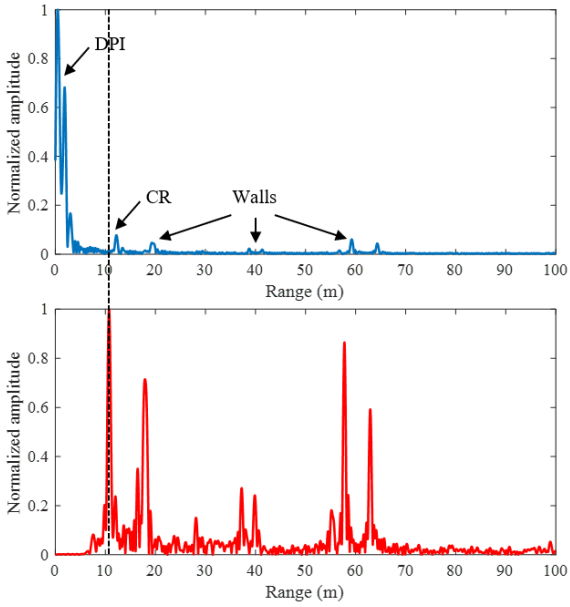

Fig. 9. Range compression results without (top) and with (bottom) DPI suppression and delay-amplitude compensation (T1/R1).

It can be seen that, without applying DPI suppression based on Eq. (24), the DPI component in the measurement channel significantly affects the target detection, especially in that shown in the top sub-figure of Fig. 10. Besides, without compensating for the delay-amplitude differences based on Eq. (26), the targets shifted from its true positions, as indicated by the vertical dashed line in the top sub-figure of Fig. 9. After conducting data preprocessing, the influences of DPI and delay-amplitude differences can be much reduced.

D. Target 2D & 3D imaging results

2D imaging result of the scene shown in the left-top sub-figure of Fig. 5 obtained by the developed SDR-GB-

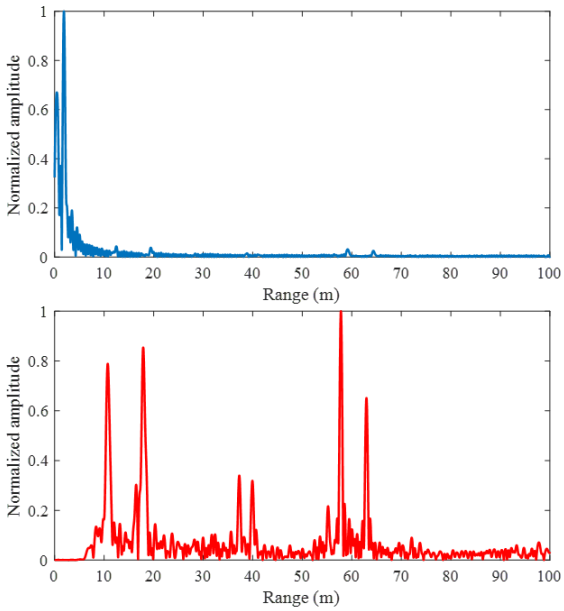

Fig. 10. Range compression results without (top) and with (bottom) DPI suppression and delay-amplitude compensation (T1/R2).

SAR system via the BPA is shown in Fig. 11, also overlaid ("freehand raster georeferencer" plugin for QGis) on an aerial photography to provide a ground truth. The system starting carrier frequency is 2400 MHz, frequency step is 1 MHz, frequency number is 100, and synthetic aperture length is 1.3 m. The transmitting antenna is set at the null radiation direction of the receiving antenna to minimize the influence of DPI. It can be seen that different targets within 100 m range can be well imaged: the house opposite of the balcony facing to the radar system is clearly visible with strong echoes from the metallic structure on the roof, while the strong reflections on the lower part are associated with discontinuities in the roof structure on top of parking boxes acting as dihedral corner reflectors, a car parked close to the radar system also acts as a strong reflector.

However, as we can see from Fig. 11, strong sidelobes exist in the obtained image, whose reason is analyzed in the sub-Section B of Section III. The proposed imaging method NUFFT-FISTA given in Table. I can thus be used to solve this problem, for which, to make it more attractive, only half (randomly selected) of the transmitted carrier frequencies are processed, giving the result shown in Fig. 12. By comparing the images obtained by different methods, it is clear that the proposed imaging method with under-sampled data can achieve better result than the BPA with full-sampled and under-sampled data: the resolution is improved and the sidelobe level is much reduced.

3D imaging result of the scene shown in the left-bottom sub-figure of Fig. 5 obtained by the TR-switched-based SDR-GB-MIMO radar system with SFCW signal via the BPA and the proposed NUFFT-FISTA are shown in Fig. 13. The system starting carrier frequency is 4850 MHz, frequency step is 1 MHz, and frequency number is 300. It can be seen that different targets within 100 m range, such as the CR and

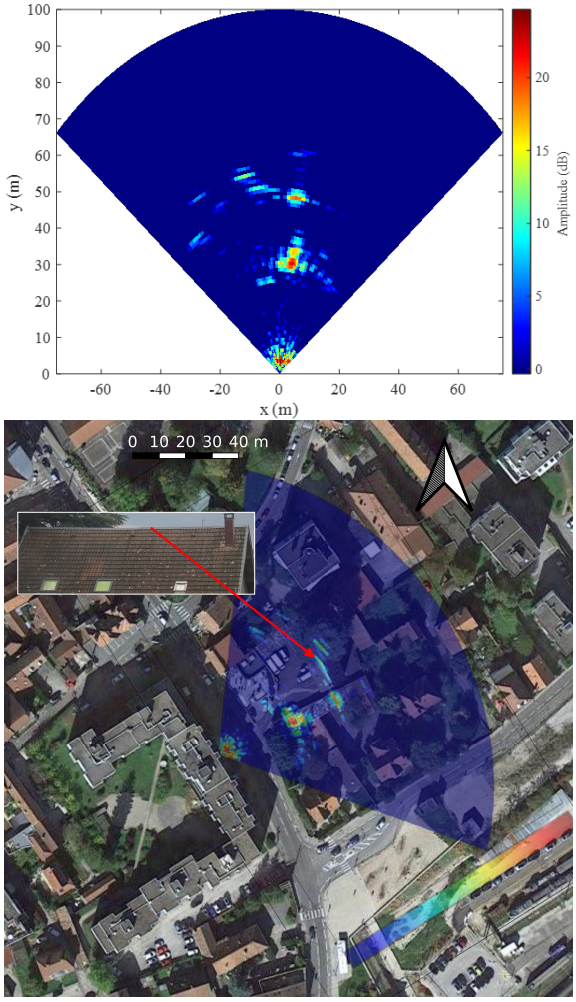

Fig. 11. Target 2D imaging result obtained by the SDR-GB-SAR system (top) and its overlay over the aerial photography (Google Maps) of the scene (bottom) as ground truth. No degree of freedom other than the orientation – defined by the rail parallel to the balcony on which the setup was installed — is available when overlapping the two images.

concrete walls, can be effectively imaged in the 3D space, which is the advantage over the 2D imaging SDR-GB-SAR system since no external digital elevation model is needed for geocoding. Besides, similar to the results shown in Fig. 11, it can also be observed that the proposed imaging method can achieve a higher-quality image than the classical BPA. To more clearly show the performance of the proposed method, a third of carrier frequencies are randomly selected for processing, resulting in the datasets displayed in Fig. 14 with the focus on the three close targets. Again, the advantage of the proposed method in sidelobe level and imaging resolution is illustrated with under-sampled data.

E. Displacement estimation and analysis

To assess the capacity of the developed system to perform displacement measurement, a trihedral CR with 30 cm-long sides was located at the scene shown in the left-top sub-figure of Fig. 5, as shown in Fig. 15, where the distance from the CR to the SDR-GB-SAR system is about 40 m. The dimensions of the CR were selected to match a 2.5 m-diameter sphere,

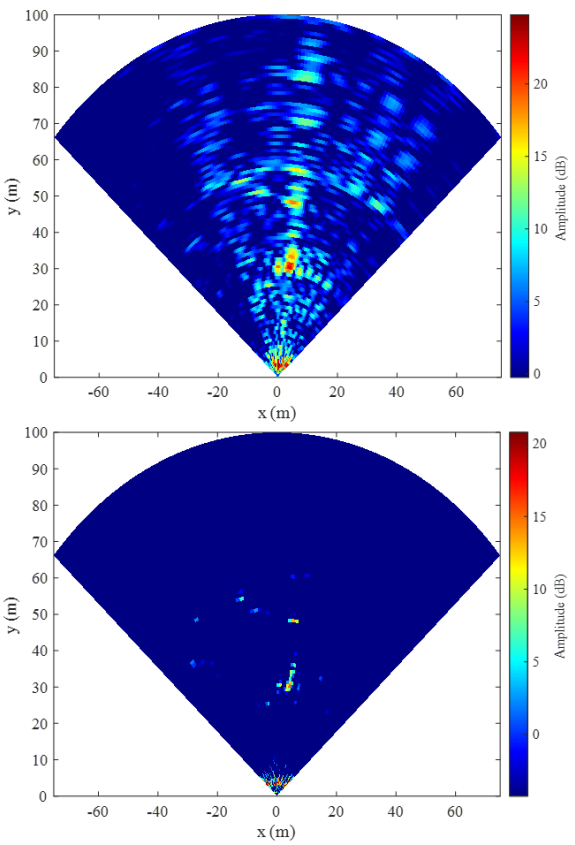

Fig. 12. Target 2D imaging result with half transmitted carrier frequencies obtained by the BPA (top) and the proposed imaging method (bottom).

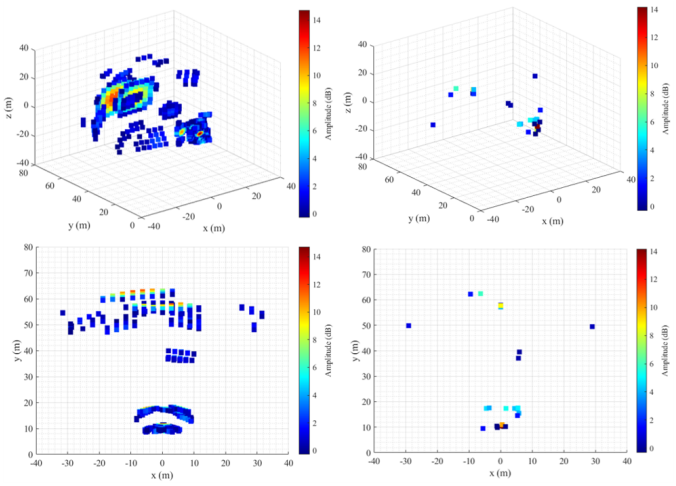

Fig. 13. Target 3D imaging result obtained by the BPA (left) and the proposed imaging method (right) with all carrier frequencies. The bottom sub-figures are the projection of the top sub-figures on the x-y coordinate

in order to provide a well resolved reflection in front of the various cars parked behind. A full acquisition lasts one hour, half of which is spend acquiring the data and half of which is needed to move the antenna along the rail.

The imaging result is shown in the left of Fig. 16, where the CR is indicated by the rectangle. Besides, to more clearly identify the location of the CR, the amplitude difference between the focused images of the scene with and without the CR is

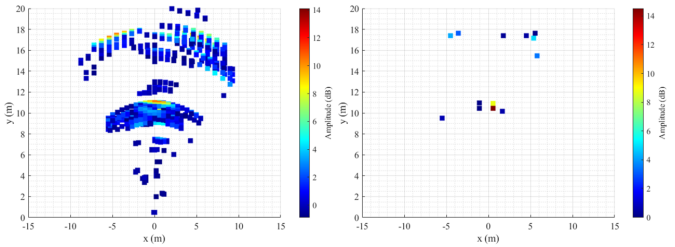

Fig. 14. Target 3D imaging result obtained by the BPA (left) and the proposed imaging method (right) with a third of carrier frequencies. The 3D images are projected on the x-y coordinate for clarity.

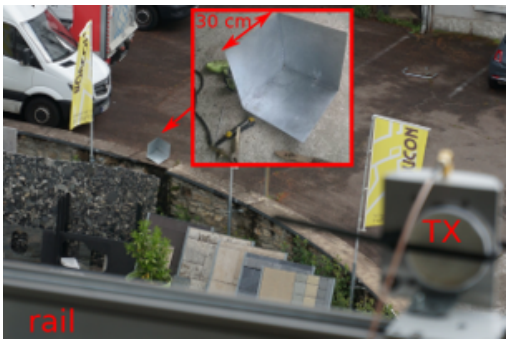

Fig. 15. The CR set in the scene for SDR-GB-SAR displacement estimation.

analyzed and shown in the right of Fig. 17, demonstrating the appear of a strong target associated with the CR.

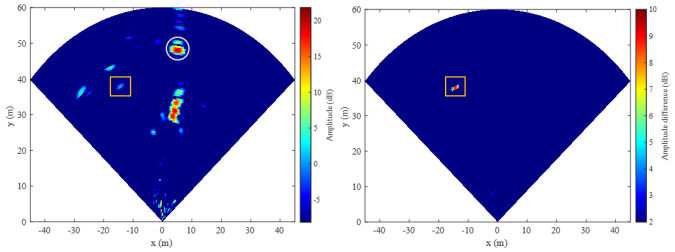

Fig. 16. Imaging result of the scene with the CR (right) and the identification of the CR via amplitude difference calculation (right).

To mimic the displacement, the CR is moved toward the radar system from 1 cm to 9 cm with a step of 1 cm. Given two adjacent measurements, Fig. 17 shows the coherence image obtained via Eq. (50) with the window size of 8×8 and the displacement map estimated by Eq. (52) for the targets with coherence values higher than 0.8 and normalized amplitudes larger than -30 dB. It can be seen that the man-made targets all have high coherence values, which hints the coherence of the developed SDR-GB-SAR system. Besides, as indicated by the rectangle in the right sub-figure of Fig. 17, the movement of the CR (1 cm) can be accurately estimated.

The accumulated displacements of the CR are then measured, as shown in Fig. 18, where the displacements of a stable point (i.e., the house roof as indicated by the circle in the left of Fig. 16, located 48.25 m away from the radar system and assumed to be static) is also plotted for comparison. Clearly, the target displacements can be accurately estimated: the root mean square errors (RMSEs) of the CR and the stable target

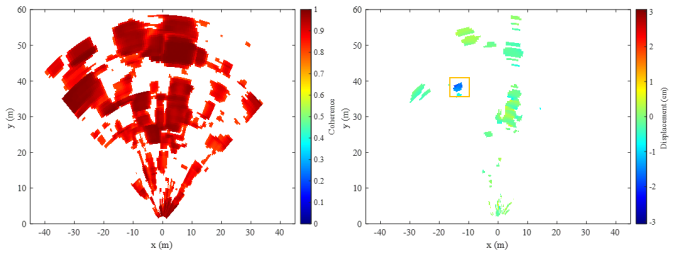

Fig. 17. Coherence image shown with a threshold of 0.8 (left) and target displacement image (left) between two adjacent measurements.

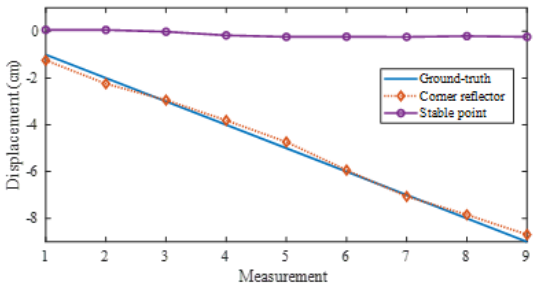

Fig. 18. Accumulated displacements of the CR and the stable house roof during ten-hours measurement.

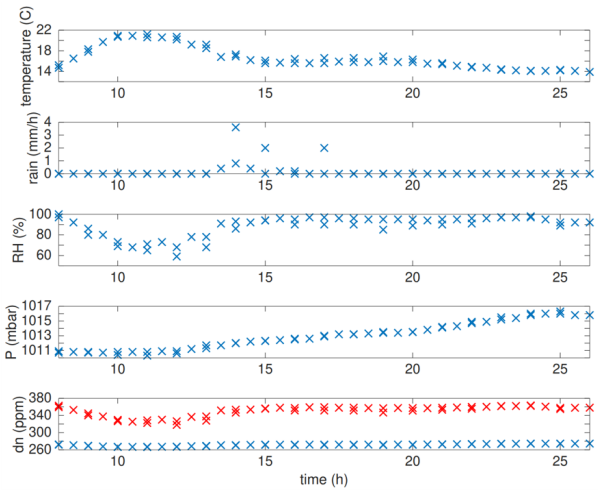

Fig. 19. Weather conditions during the day the displacement measurement was completed, and the resulting optical index variation (bottom) in ppm with respect to the velocity of light in vacuum.

are 1.99 mm and 1.86 mm, respectively. In the following, we try to explain where the errors come from.

While the variation of the velocity of light in air as a function of weather condition is negligible for range measurement, it becomes dramatic for displacement measurement. Actually, a 2-mm error of displacement estimation means measuring 41.5 ppm relative range variations. Optical index of the atmosphere, defining the velocity of light variation to its velocity in vacuum, is mostly driven by the temperature, pressure and relative moisture [48]. These parameters have been recorded, as found at [49], during the day the measurement of Fig. 18 was collected, as shown in Fig. 19. We can conclude from this figure that, beyond the mean optical index offset of a few hundreds of ppm consistent with the literature [50], a variation of 41.5 ppm can be mostly justified from the moisture level variations over the day. Actually, for long-term displacement monitoring by GBIR, a fixed CR located at a place known to be not moved is classically used as reference for measuring the optical index of air and canceling the impact of weather on the measurement results [2].

F. Implementation based on Wi-Fi signals

At last, we demonstrate the development flexibility of the SDR-GBIR system by replacing the PlutoSDR emitter with a Wi-Fi USB dongle. Actually, since no FPGA firmware needs to be modified, any SDR transmitter and receiver with at least two coherent channels can be used for SDR-GBIR to enjoy the desired characteristics of different SDR platforms. Compared to PlutoSDR, a Wi-Fi emitter can provide the following two significant benefits: 1) meeting radiofrequency emission regulations and combining radar measurement with digital communication, making SDR-GBIR well suited for monitoring displacement in urban conditions with little or no disturbance to existing infrastructures; 2) allowing for a bigger carrier frequency step than the PlutoSDR transmission that is limited by the communication bandwidth of 2.7 MHz without loss of samples since the used Wi-Fi channels are separated by 5 MHz. Indeed the sampling rate is now only limited by the B210 communication over the USB-3 interface as the slower PlutoSDR is no longer the limiting factor: throughout the experiments with a Wi-Fi emitter, a sampling rate of 5 MHz is used. In our demonstration, despite the near continuous Wi-Fi emission thanks to the software available at [51] that requires a Wi-Fi chipset compatible with the monitoring mode, the successive Wi-Fi packets and associated radiofrequency emissions are observed to be discontinuous. Under such conditions, the reference channel power is monitored and the data collected from the ZeroMQ stream is only saved when this power is above a threshold.

Similar to the frequency-modulated signal and the phase-coded signal, the OFDM approach employed by the Wi-Fi signal is also a popular way to increase the bandwidth in each TR routine, and hence can be applied for bandwidth synthesis in SDR-GBIR to get an increased detection range than the SFCW signal. In this study, 11 channels of the IEEE 802.11 2.4 GHz Wi-Fi signal, separated by 5 MHz each, are applied to get a range resolution of about 2.7 m. The spectrum of a 2412 MHz Wi-Fi channel is shown in Fig. 20, from which it can be learned that, different from the noise signal spectrum shown in Fig. 7, the OFDW Wi-Fi signal has multiple sub-carriers separated by 312.5 kHz with the missing sub-carrier 0 at the center frequency. In order to avoid the strong spectral feature of the unused sub-carrier 0 at the center frequency of each Wi-Fi channel, the local oscillator of the B210 receiver is offset by 3 MHz with respect to the Wi-Fi transmitter, and thus a 5 MHz bandwidth signal can be collected in each TR routine, as shown in Fig. 21.

Finally, with the Wi-Fi transmitted signal and a 2.0 m synthetic aperture length, imaging results of the same scene shown in the left-top sub-figure of Fig. 5 are obtained by the

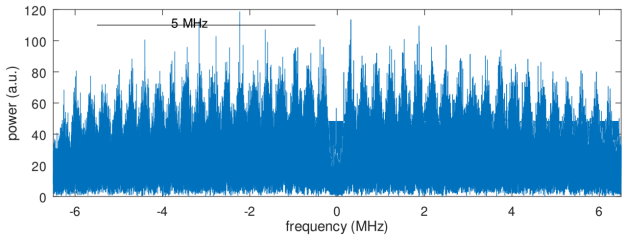

Fig. 20. Spectrum of a Wi-Fi channel emphasizing the OFDM sub-carrier structure separated by 312.5 kHz steps with the missing sub-carrier 0 at center frequency. The indicated 5 MHz spectrum is actually sampled.

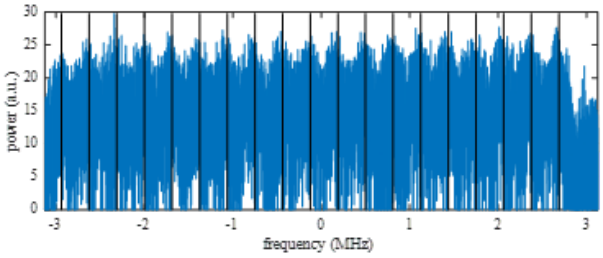

Fig. 21. A 5 MHz wide usable spectrum is collected by offsetting the local oscillators between the B210 receiver and the Wi-Fi transmitter to avoid the missing sub-carrier 0: The Wi-Fi local oscillator is at $2412+5(q-1)$ MHz, while the B210 local oscillator is set to 3 MHz below. The vertical lines indicate 19 sub-carriers.

BPA and the proposed imaging method, as shown in Fig. 22. It can be seen that, despite the lower range resolution (2.7 m v.s. 1.5 m) and higher azimuth resolution (0.031 v.s. 0.047), different targets are clearly visible and well consistent with the results obtained by transmitting the NW signal, as shown in Figs. 11 and 12, hence demonstrating the suitability of replacing the PlutoSDR emitter with the Wi-Fi USB dongle for SDR-GBIR development.

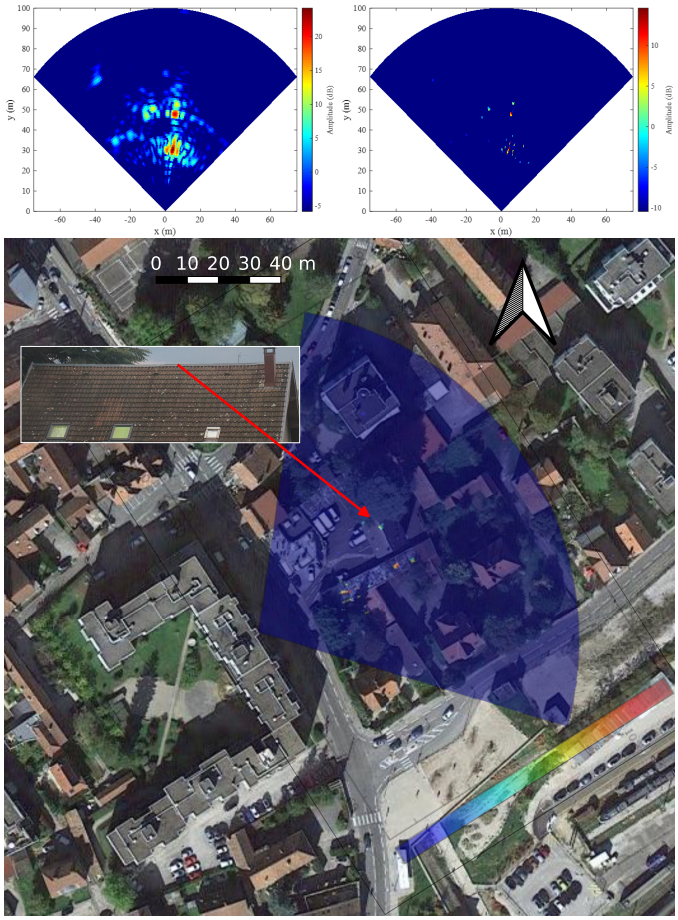

Fig. 22. Top: imaging results of the same scene as shown in Figs. 11 and 12 by transmitting the Wi-Fi signal, obtained by the BPA (left) and the proposed imaging method (right). Bottom: the echo map is overlaid over an aerial picture (Google Maps) as ground truth.

V. Conclusion

We have demonstrated the software defined radio implementation of ground-based interferometric radar by addressing the challenges of system synchronization, bandwidth synthesis, data preprocessing, and signal processing. The developed SDR-GB-SAR and SDR-GB-MIMO radar systems have been validated to work well in practice using the proposed methods for target high-resolution imaging and displacement high-accuracy measurement, enjoying the potentials to reduce the cost and increase the flexibility of current radar systems in the same application field. The setup is furthermore well suited for educational purposes as it only requires widely available and affordable commercial off the shelf hardware, e.g., PlutoSDR or Wi-Fi USB dongle as transmitter, B210 as receiver, and a couple of passive components such as coupler and attenuators in addition to the antennas. All source codes and some datasets resulting from this work are available on the https://github.com/jmfriedt/active_radar Github repository.

Acknowledgements

P. Abbé (FEMTO-ST Time & Frequency, France) assembled the corner reflector displayed in Fig. 15. H. Boeglen (XLim, Poitiers, France) described the Wi-Fi signal structure. This work was partly supported by the Oscillator Instability Measurement Platform (OscillatorIMP) grant from the French National Research Agency as well as the National Natural Science Foundation of China under Grant 62001507.

References

[1] O Monserrat, M Crosetto, and G Luzi, "A review of ground-based SAR interferometry for deformation measurement," *ISPRS Journal of Photogrammetry and Remote Sensing*, vol. 93, pp. 40–48, 2014.

[2] Guido Luzi, Massimiliano Pieraccini, Daniele Mecatti, Linhsia Noferini, Gabriele Guidi, Fabio Moia, and Carlo Atzeni, "Ground-based radar interferometry for landslides monitoring: atmospheric and instrumental decorrelation sources on experimental data," *IEEE transactions on geoscience and remote sensing*, vol. 42, no. 11, pp. 2454–2466, 2004.

[3] Weike Feng, Giovanni Nico, and Motoyuki Sato, "GB-SAR interferometry based on dimension-reduced compressive sensing and multiple measurement vectors model," *IEEE Geoscience and Remote Sensing Letters*, vol. 16, no. 1, pp. 70–74, 2018.

[4] Massimiliano Pieraccini and Lapo Miccinesi, "Ground-based radar interferometry: A bibliographic review," *Remote Sensing*, vol. 11, no. 9, pp. 1029, 2019.

[5] Ashutosh Tiwari, Avadh Bihari Narayan, Ramji Dwivedi, Onkar Dikshit, and B Nagarajan, "Monitoring of landslide activity at the Sirobagarh landslide, Uttarakhand, India, using LiDAR, SAR interferometry and geodetic surveys," *Geocarto International*, vol. 35, no. 5, pp. 535–558, 2020.

[6] Charles Elachi, Tom Bicknell, Rolando L Jordan, and Chialin Wu, "Spaceborne synthetic-aperture imaging radars: Applications, techniques, and technology," *Proceedings of the IEEE*, vol. 70, no. 10, pp. 1174–1209, 1982.

[7] Michele Crosetto, Oriol Monserrat, María Cuevas, and Bruno Crippa, "Spaceborne differential SAR interferometry: Data analysis tools for deformation measurement," *Remote Sensing*, vol. 3, no. 2, pp. 305–318, 2011.

[8] Yuan Gao, Mohammad Tayeb Ghasr, and Reza Zoughi, "Effects of and compensation for translational position error in microwave synthetic aperture radar imaging systems," *IEEE Transactions on Instrumentation and Measurement*, vol. 69, no. 4, pp. 1205–1212, 2019.

[9] Jian Li and Petre Stoica, "MIMO radar with colocated antennas," *IEEE Signal Processing Magazine*, vol. 24, no. 5, pp. 106–114, 2007.

[10] Dario Tarchi, Nicola Casagli, Sandro Moretti, Davide Leva, and Alois J Sieber, "Monitoring landslide displacements by using ground-based synthetic aperture radar interferometry: Application to the ruinon landslide in the italian alps," *Journal of Geophysical Research: Solid Earth*, vol. 108, no. B8, 2003.

[11] Sabine Rödelsperger, Gwendolyn Läufer, Carl Gerstenecker, and Matthias Becker, "Monitoring of displacements with ground-based microwave interferometry: IBIS-S and IBIS-L," *Journal of Applied Geodesy*, vol. 4, no. 1, pp. 41–54, 2010.

[12] Sabine Rödelsperger and Adriano Meta, "MetaSensing's FastGBSAR: ground based radar for deformation monitoring," in *SAR Image Analysis, Modeling, and Techniques XIV*. International Society for Optics and Photonics, 2014, vol. 9243, p. 924318.

[13] Konstantin Lukin, Anatoliy Mogyla, Vladimir Palamarchuk, Pavlo Vyplavin, Evgeniy Kozhan, and Sergey Lukin, "Monitoring of St. Sophia Cathedral interior using Ka-band ground based noise waveform sar," in *2009 European Radar Conference (EuRAD)*. IEEE, 2009, pp. 215–217.

[14] Yunhua Luo, Hongjun Song, Robert Wang, Yunkai Deng, Fengjun Zhao, and Zheng Xu, "Arc FMCW SAR and applications in ground monitoring," *IEEE Transactions on Geoscience and Remote Sensing*, vol. 52, no. 9, pp. 5989–5998, 2014.

[15] Joan Broussolle, Vladimir Kyovtorov, Marco Basso, Guido Ferraro Di Silvi E Castiglione, Jorge Figueiredo Morgado, Raimondo Giuliani, Franco Oliveri, Pier Francesco Sammartino, and Dario Tarchi, "MELISSA, a new class of ground based InSAR system. an example of application in support to the costa concordia emergency," *ISPRS journal of photogrammetry and remote sensing*, vol. 91, pp. 50–58, 2014.

[16] Cheng Hu, Jingyang Wang, Weiming Tian, Tao Zeng, and Rui Wang, "Design and imaging of ground-based multiple-input multiple-output synthetic aperture radar (MIMO SAR) with non-collinear arrays," *Sensors*, vol. 17, no. 3, pp. 598, 2017.

[17] Alberto Michelini, Francesco Coppi, Alberto Bicci, and Giovanni Alli, "SPARX, a MIMO array for ground-based radar interferometry," *Sensors*, vol. 19, no. 2, pp. 252, 2019.

[18] Massimiliano Pieraccini and Lapo Miccinesi, "An interferometric MIMO radar for bridge monitoring," *IEEE Geoscience and Remote Sensing Letters*, vol. 16, no. 9, pp. 1383–1387, 2019.

[19] Weike Feng, Jean-Michel Friedt, Giovanni Nico, and Motoyuki Sato, "3-D ground-based imaging radar based on C-band cross-MIMO array and tensor compressive sensing," *IEEE Geoscience and Remote Sensing Letters*, vol. 16, no. 10, pp. 1585–1589, 2019.

[20] Sevgi Zubeyde Gurbuz, Hugh D Griffiths, Alexander Charlish, Muralidhar Rangaswamy, Maria Sabrina Greco, and Kristine Bell, "An overview of cognitive radar: Past, present, and future," *IEEE Aerospace and Electronic Systems Magazine*, vol. 34, no. 12, pp. 6–18, 2019.

[21] Maria S Greco, Fulvio Gini, Pietro Stinco, and Kristine Bell, "Cognitive radars: On the road to reality: Progress thus far and possibilities for the future," *IEEE Signal Processing Magazine*, vol. 35, no. 4, pp. 112–125, 2018.

[22] Tonmo V Fepeussi, Nicolo Testi, Yang Xu, and Yuanwei Jin, "High-accuracy narrowband software-defined radar using successive multiple-frequency continuous-wave modulation for sensing applications," *IEEE Transactions on Microwave Theory and Techniques*, vol. 67, no. 9, pp. 3917–3927, 2019.

[23] John Meier, Redmond Kelley, Bradley M Isom, Mark Yeary, and Robert D Palmer, "Leveraging software-defined radio techniques in multichannel digital weather radar receiver design," *IEEE Transactions on Instrumentation and Measurement*, vol. 61, no. 6, pp. 1571–1582, 2012.

[24] Samuel Prager, Tushar Thrivikraman, Mark S Haynes, John Stang, David Hawkins, and Mahta Moghaddam, "Ultrawideband synthesis for high-range-resolution software-defined radar," *IEEE Transactions on Instrumentation and Measurement*, vol. 69, no. 6, pp. 3789–3803, 2019.

[25] Gregory L Charvat, *Small and short-range radar systems*, CRC Press, 2014.

[26] Weike Feng, Jean-Michel Friedt, Grigory Cherniak, Zhipeng Hu, and Motoyuki Sato, "Direct path interference suppression for short-range passive bistatic synthetic aperture radar imaging based on atomic norm minimisation and vandermonde decomposition," *IET Radar, Sonar & Navigation*, vol. 13, no. 7, pp. 1171–1179, 2019.

[27] Joseph Landon Garry, Chris J Baker, and Graeme E Smith, "Evaluation of direct signal suppression for passive radar," *IEEE Transactions on Geoscience and Remote Sensing*, vol. 55, no. 7, pp. 3786–3799, 2017.

[28] Philipp Wojaczek, Fabiola Colone, Diego Cristallini, and Pierfrancesco Lombardo, "Reciprocal-filter-based STAP for passive radar on moving platforms," *IEEE Transactions on Aerospace and Electronic Systems*, vol. 55, no. 2, pp. 967–988, 2018.

[29] Ya-Wei Wang, Guang-Ming Wang, and Bin-Feng Zong, "Directivity improvement of Vivaldi antenna using double-slot structure," *IEEE Antennas and Wireless Propagation Letters*, vol. 12, pp. 1380–1383, 2013.

[30] Jean-Michel Friedt and Weike Feng, "Software defined radio based synthetic aperture noise and OFDM (Wi-Fi) RADAR mapping," in *Proceedings of the 10th GNU Radio Conference*, 2020, vol. 5.

[31] Donald R Wehner, "High resolution radar," *ah*, 1987.

[32] H Schimpf, A Wahlen, and H Essen, "High range resolution by means of synthetic bandwidth generated by frequency-stepped chirps," *Electronics Letters*, vol. 39, no. 18, pp. 1346–1348, 2003.

[33] MA Temple, KL Sitler, RA Raines, and JA Hughes, "High range resolution (HRR) improvement using synthetic HRR processing and stepped-frequency polyphase coding," *IEE Proceedings-Radar, Sonar and Navigation*, vol. 151, no. 1, pp. 41–47, 2004.

[34] Inc. Analog Devices, ," https://github.com/analogdevicesinc/gr-iio/tree/single-param.

[35] Joaquim Fortuny-Guasch, "A fast and accurate far-field pseudopolar format radar imaging algorithm," *IEEE transactions on geoscience and remote sensing*, vol. 47, no. 4, pp. 1187–1196, 2009.

[36] Pietro Guccione, Mariantonietta Zonno, Luigi Mascolo, and Giovanni Nico, "Focusing algorithms analysis for ground-based SAR images," in *2013 IEEE International Geoscience and Remote Sensing Symposium-IGARSS*. IEEE, 2013, pp. 3895–3898.

[37] Dario Tarchi, Franco Oliveri, and Pier Francesco Sammartino, "MIMO radar and ground-based SAR imaging systems: Equivalent approaches for remote sensing," *IEEE Transactions on Geoscience and Remote Sensing*, vol. 51, no. 1, pp. 425–435, 2012.

[38] Baolong Wu and Lei He, "Multi-layered circular dielectric structure sar imaging based on compressed sensing for FOD Detection in NDT," *IEEE Transactions on Instrumentation and Measurement*, 2020.

[39] Ingrid Daubechies, Michel Defrise, and Christine De Mol, "An iterative thresholding algorithm for linear inverse problems with a sparsity constraint," *Communications on Pure and Applied Mathematics: A Journal Issued by the Courant Institute of Mathematical Sciences*, vol. 57, no. 11, pp. 1413–1457, 2004.

[40] Amir Beck and Marc Teboulle, "A fast iterative shrinkage-thresholding algorithm for linear inverse problems," *SIAM journal on imaging sciences*, vol. 2, no. 1, pp. 183–202, 2009.

[41] Jian Fang, Zongben Xu, Bingchen Zhang, Wen Hong, and Yirong Wu, "Fast compressed sensing SAR imaging based on approximated observation," *IEEE Journal of Selected Topics in Applied Earth Observations and Remote Sensing*, vol. 7, no. 1, pp. 352–363, 2013.

[42] Hui Bi, Bingchen Zhang, Xiao Xiang Zhu, Chenglong Jiang, and Wen Hong, "Extended chirp scaling-baseband azimuth scaling-based azimuth–range decouple $l\_\{1\}$ regularization for TOPS SAR imaging via CAMP," *IEEE Transactions on Geoscience and Remote Sensing*, vol. 55, no. 7, pp. 3748–3763, 2017.

[43] Leslie Greengard and June-Yub Lee, "Accelerating the nonuniform fast Fourier transform," *SIAM review*, vol. 46, no. 3, pp. 443–454, 2004.

[44] CMCL, ," https://cims.nyu.edu/cmcl/nufft/nufft.html.

[45] Alok Dutt and Vladimir Rokhlin, "Fast fourier transforms for nonequispaced data," *SIAM Journal on Scientific computing*, vol. 14, no. 6, pp. 1368–1393, 1993.

[46] June-Yub Lee and Leslie Greengard, "The type 3 nonuniform FFT and its applications," *Journal of Computational Physics*, vol. 206, no. 1, pp. 1 – 5, 2005.

[47] Ramon F Hanssen, *Radar interferometry: data interpretation and error analysis*, vol. 2, Springer Science & Business Media, 2001.

[48] E. K. Smith and S. Weintraub, "The constants in the equation for atmospheric refractive index at radio frequencies," *Proceedings of the IRE*, vol. 41, no. 8, pp. 1035–1037, 1953.

[49] meteo, ," https://www.infoclimat.fr/observations-meteo/archives/13/juin/2020/besancon/000P2.html.
[50] Frédéric Fabry, "Meteorological value of ground target measurements by radar," *Journal of Atmospheric and Oceanic Technology*, vol. 21, no. 4, pp. 560–573, 2004.
[51] B. Bloessl, ," github.com/bastibl/gr-ieee802-11/tree/maint-3.8/utils/packetspammer.